UNIVERSITY OF AMSTERDAM

UvA-DARE (Digital Academic Repository)

Observation of the Gamma-Ray Binary HESS J0632+057 with the H.E.S.S., MAGIC, and VERITAS Telescopes

Adams, C.B.; Prokhorov, D.A.; Simoni, R. ; Sun, L.; Vink, J.; Moritani, Y.; Torres, D.F.; The VERITAS Collaboration; The MAGIC collaboration; The H.E.S.S. Collaboration

DOI
10.3847/1538-4357/ac29b7

Publication date
2021

Document Version
Final published version

Published in
Astrophysical Journal

License
CC BY

Link to publication

Citation for published version (APA):
Adams, C. B., Prokhorov, D. A., Simoni, R., Sun, L., Vink, J., Moritani, Y., Torres, D. F., The VERITAS Collaboration, The MAGIC collaboration, & The H.E.S.S. Collaboration (2021). Observation of the Gamma-Ray Binary HESS J0632+057 with the H.E.S.S., MAGIC, and VERITAS Telescopes. *Astrophysical Journal*, *923*(2), Article 241. https://doi.org/10.3847/1538-4357/ac29b7

General rights
It is not permitted to download or to forward/distribute the text or part of it without the consent of the author(s) and/or copyright holder(s), other than for strictly personal, individual use, unless the work is under an open content license (like Creative Commons).

Disclaimer/Complaints regulations
If you believe that digital publication of certain material infringes any of your rights or (privacy) interests, please let the Library know, stating your reasons. In case of a legitimate complaint, the Library will make the material inaccessible and/or remove it from the website. Please Ask the Library: https://uba.uva.nl/en/contact, or a letter to: Library of the University of Amsterdam, Secretariat, P.O. Box 19185, 1000 GD Amsterdam, The Netherlands. You will be contacted as soon as possible.
UvA-DARE is a service provided by the library of the University of Amsterdam (https://dare.uva.nl)

Download date:13 Oct 2026

The Astrophysical Journal, 923:241 (30pp), 2021 December 20 https://doi.org/10.3847/1538-4357/ac29b7
© 2021. The Author(s). Published by the American Astronomical Society.
OPEN ACCESS

Observation of the Gamma-Ray Binary HESS J0632+057 with the H.E.S.S., MAGIC, and VERITAS Telescopes

C. B. Adams[1], W. Benbow[2], A. Brill[1], J. H. Buckley[3], M. Capasso[4], A. J. Chromey[5], M. Errando[3], A. Falcone[6], K. A Farrell[7], Q. Feng[4], J. P. Finley[8], G. M Foote[9], L. Fortson[10], A. Furniss[11], A. Gent[12], G. H. Gillanders[13], C. Giuri[14], O. Gueta[14], D. Hanna[15], T. Hassan[14], O. Hervet[16], J. Holder[9], B. Hona[17], T. B. Humensky[1], W. Jin[18], P. Kaaret[19], M. Kertzman[20], D. Kieda[17], T. K Kleiner[14], F. Krennrich[5], S. Kumar[15], M. J. Lang[13], M. Lundy[15], G. Maier[14,118], C. E McGrath[7], P. Moriarty[13], R. Mukherjee[4], D. Nieto[21], M. Nievas-Rosillo[14], S. O'Brien[15], R. A. Ong[22], A. N. Otte[12], N. Park[23], S. Patel[19], K. Pfrang[14], A. Pichel[24], M. Pohl[14,25], R. R. Prado[14], J. Quinn[7], K. Ragan[15], P. T. Reynolds[26], D. Ribeiro[1], E. Roache[2], A. C. Rovero[24], J. L. Ryan[22], M. Santander[18], S. Schlenstedt[27], G. H. Sembroski[8], R. Shang[22], D. Tak[14], V. V. Vassiliev[22], A. Weinstein[5], D. A. Williams[16], T. J Williamson[9]
(The VERITAS Collaboration)

V. A. Acciari[28], S. Ansoldi[29,30], L. A. Antonelli[31], A. Arbet Engels[32], M. Artero[33], K. Asano[34], D. Baack[35], A. Babić[36], A. Baquero[37], U. Barres de Almeida[38], J. A. Barrio[37], I. Batković[39], J. Becerra González[28], W. Bednarek[40], L. Bellizzi[41], E. Bernardini[42], M. Bernardos[39], A. Berti[43], J. Besenrieder[43], W. Bhattacharyya[42], C. Bigongiari[31], A. Biland[32], O. Blanch[33], H. Bökenkamp[35], G. Bonnoli[41], Ž. Bošnjak[36], G. Busetto[39], R. Carosi[44], G. Ceribella[43], M. Cerruti[45], Y. Chai[43], A. Chilingarian[46], S. Cikota[36], S. M. Colak[33], E. Colombo[28], J. L. Contreras[37], J. Cortina[47], S. Covino[31], G. D'Amico[43,48], V. D'Elia[31], P. Da Vela[44,49], F. Dazzi[31], A. De Angelis[39], B. De Lotto[29], M. Delfino[33,50], J. Delgado[33,50], C. Delgado Mendez[47], D. Depaoli[51], F. Di Pierro[51], L. Di Venere[52], E. Do Souto Espiñeira[33], D. Dominis Prester[53], A. Donini[29], D. Dorner[54], M. Doro[39], D. Elsaesser[35], V. Fallah Ramazani[55,56], A. Fattorini[35], M. V. Fonseca[37], L. Font[57], C. Fruck[43], S. Fukami[34], Y. Fukazawa[58], R. J. García López[28], M. Garczarczyk[42], S. Gasparyan[59], M. Gaug[57], N. Giglietto[52], F. Giordano[52], P. Gliwny[40], N. Godinović[60], J. G. Green[31], D. Green[43], D. Hadasch[34,118], A. Hahn[43], L. Heckmann[43], J. Herrera[28], J. Hoang[37,61], D. Hrupec[62], M. Hütten[43], T. Inada[34], K. Ishio[43], Y. Iwamura[34], I. Jiménez Martínez[47], J. Jormanainen[55], L. Jouvin[33], M. Karjalainen[28], D. Kerszberg[33], Y. Kobayashi[34], H. Kubo[63], J. Kushida[64], A. Lamastra[31], D. Lelas[60], F. Leone[31], E. Lindfors[55], L. Linhoff[35], S. Lombardi[31], F. Longo[29,65], R. López-Coto[39], M. López-Moya[37], A. López-Oramas[28,118], S. Loporchio[52], B. Machado de Oliveira Fraga[38], C. Maggio[57], P. Majumdar[66], M. Makariev[67], M. Mallamaci[39], G. Maneva[67], M. Manganaro[53], K. Mannheim[54], L. Maraschi[31], M. Mariotti[39], M. Martínez[33], D. Mazin[34,43], S. Menchiari[41], S. Mender[35], S. Mićanović[53], D. Miceli[29,68], T. Miener[37], J. M. Miranda[41], R. Mirzoyan[43], E. Molina[45], A. Moralejo[33], D. Morcuende[37], V. Moreno[57], E. Moretti[33], T. Nakamori[69], L. Nava[31], V. Neustroev[70], C. Nigro[33], K. Nilsson[55], K. Nishijima[64], K. Noda[34], S. Nozaki[63], Y. Ohtani[34], T. Oka[63], J. Otero-Santos[28], S. Paiano[31], M. Palatiello[29], D. Paneque[43], R. Paoletti[41], J. M. Paredes[45], L. Pavletić[53], P. Peñil[37], M. Persic[29,71], M. Pihet[43], P. G. Prada Moroni[44], E. Prandini[39], C. Priyadarshi[33], I. Puljak[60], W. Rhode[35], M. Ribó[45], J. Rico[33], C. Righi[31], A. Rugliancich[44], L. Saha[37], N. Sahakyan[59], T. Saito[34], S. Sakurai[34], K. Satalecka[42], F. G. Saturni[31], B. Schleicher[54], K. Schmidt[35], T. Schweizer[43], J. Sitarek[40], I. Šnidarić[72], D. Sobczynska[40], A. Spolon[39], A. Stamerra[31], J. Strišković[62], D. Strom[43], M. Strzys[34], Y. Suda[58], T. Surić[72], M. Takahashi[34], R. Takeishi[34], F. Tavecchio[31], P. Temnikov[67], T. Terzić[53], M. Teshima[34,43], L. Tosti[73], S. Truzzi[41], A. Tutone[31], S. Ubach[57], J. van Scherpenberg[43], G. Vanzo[28], M. Vazquez Acosta[28], S. Ventura[41], V. Verguilov[67], C. F. Vigorito[51], V. Vitale[74], I. Vovk[34], M. Will[43], C. Wunderlich[41], T. Yamamoto[75], D. Zarić[60]
(The MAGIC collaboration)

H. Abdalla[76], F. Aharonian[77,78,79], F. Ait Benkhali[78], E. O. Angüner[80], C. Arcaro[81], H. Ashkar[82], M. Backes[76,81], V. Barbosa Martins[83], M. Barnard[81], R. Batzofin[84], Y. Becherini[85], D. Berge[83], K. Bernlöhr[78], B. Bi[86], M. Böttcher[81], C. Boisson[87], J. Bolmont[88], M. de Bony de Lavergne[89], M. Breuhaus[78], R. Brose[77], F. Brun[82], T. Bulik[90], S. Caroff[88], S. Casanova[91], T. Chand[81], A. Chen[84], G. Cotter[92], J. Damascenev Mbarubucyeye[83], J. Devin[93], A. Djannati-Ataï[94], K. Egberts[95], J.-P. Ernenwein[80], S. Fegan[96], A. Fiasson[89], G. Fichet de Clairfontaine[87], G. Fontaine[96], M. Füßling[83], S. Funk[97], S. Gabici[94], G. Giavitto[83], D. Glawion[97], J. F. Glicenstein[82], M.-H. Grondin[93], J. A. Hinton[78], W. Hofmann[78], T. L. Holch[83], M. Holler[98], D. Horns[99], Zhiqiu Huang[78], M. Jamrozy[100], F. Jankowsky[101], V. Joshi[97], I. Jung-Richardt[97], E. Kasai[76], K. Katarzyński[102], B. Khélifi[94], Nu. Komin[84], K. Kosack[82], D. Kostunin[83], S. Le Stum[80], A. Lemière[94], J.-P. Lenain[88], F. Leuschner[86], C. Levy[88], T. Lohse[103], A. Luashvili[87], I. Lypova[101], J. Mackey[77], J. Majumdar[83], D. Malyshev[86,118], V. Marandon[78], P. Marchegiani[84], A. Marcowith[104], G. Martí-Devesa[98], R. Marx[101], G. Maurin[89], P. J. Meintjes[105], A. Mitchell[78], R. Moderski[106], L. Mohrmann[97], A. Montanari[82], E. Moulin[82], J. Muller[96], T. Murach[83], M. de Naurois[96], A. Nayerhoda[91], J. Niemiec[118], A. Priyana Noel[100], P. O'Brien[107], S. Ohm[83], L. Olivera-Nieto[78], E. de Ona Wilhelmi[83], M. Ostrowski[100], S. Panny[98], M. Panter[78], R. D. Parsons[103], G. Peron[78],

V. Poireau[89], D. A. Prokhorov[108], H. Prokoph[83], G. Pühlhofer[86,118], M. Punch[85,94], A. Quirrenbach[101], P. Reichherzer[82], A. Reimer[98], O. Reimer[98], M. Renaud[104], F. Rieger[78], C. Romoli[78], G. Rowell[109], B. Rudak[106], H. Rueda Ricarte[82], E. Ruiz-Velasco[78], V. Sahakian[110], S. Sailer[78], H. Salzmann[86], D. A. Sanchez[89], A. Santangelo[86], M. Sasaki[97], H. M. Schutte[81], U. Schwanke[103], F. Schüssler[82], M. Senniappan[85], J. N. S. Shapopi[76], R. Simoni[108], H. Sol[87], A. Specovius[97], S. Spencer[92], R. Steenkamp[76], S. Steinmassl[78], L. Sun[108], T. Takahashi[111], T. Tanaka[112], R. Terrier[94], N. Tsuji[113], Y. Uchiyama[114], C. van Eldik[97], B. van Soelen[105], J. Veh[97], C. Venter[81], J. Vink[108], S. J. Wagner[101], R. White[78], A. Wierzcholska[91], Yu Wun Wong[97], M. Zacharias[87], D. Zargaryan[77,79], A. A. Zdziarski[106], A. Zech[87], S. J. Zhu[83], S. Zouari[94], N. Żywucka[81]
(The H.E.S.S. Collaboration)

Y. Moritani[111], and D. F. Torres[115,116,117]
[1] Physics Department, Columbia University, New York, NY 10027, USA
[2] Center for Astrophysics | Harvard & Smithsonian, Cambridge, MA 02138, USA
[3] Department of Physics, Washington University, St. Louis, MO 63130, USA
[4] Department of Physics and Astronomy, Barnard College, Columbia University, NY 10027, USA
[5] Department of Physics and Astronomy, Iowa State University, Ames, IA 50011, USA
[6] Department of Astronomy and Astrophysics, 525 Davey Lab, Pennsylvania State University, University Park, PA 16802, USA
[7] School of Physics, University College Dublin, Belfield, Dublin 4, Ireland
[8] Department of Physics and Astronomy, Purdue University, West Lafayette, IN 47907, USA
[9] Department of Physics and Astronomy and the Bartol Research Institute, University of Delaware, Newark, DE 19716, USA
[10] School of Physics and Astronomy, University of Minnesota, Minneapolis, MN 55455, USA
[11] Department of Physics, California State University—East Bay, Hayward, CA 94542, USA
[12] School of Physics and Center for Relativistic Astrophysics, Georgia Institute of Technology, 837 State Street NW, Atlanta, GA 30332-0430, USA
[13] School of Physics, National University of Ireland Galway, University Road, Galway, Ireland
[14] DESY, Platanenallee 6, 15738 Zeuthen, Germany
[15] Physics Department, McGill University, Montreal, QC H3A 2T8, Canada
[16] Santa Cruz Institute for Particle Physics and Department of Physics, University of California, Santa Cruz, CA 95064, USA
[17] Department of Physics and Astronomy, University of Utah, Salt Lake City, UT 84112, USA
[18] Department of Physics and Astronomy, University of Alabama, Tuscaloosa, AL 35487, USA
[19] Department of Physics and Astronomy, University of Iowa, Van Allen Hall, Iowa City, IA 52242, USA
[20] Department of Physics and Astronomy, DePauw University, Greencastle, IN 46135-0037, USA
[21] Institute of Particle and Cosmos Physics, Universidad Complutense de Madrid, E-28040 Madrid, Spain
[22] Department of Physics and Astronomy, University of California, Los Angeles, CA 90095, USA
[23] Department of Physics, Queen's University, Kingston, ON K7L 3N6, Canada
[24] Instituto de Astronomía y Física del Espacio (IAFE, CONICET-UBA), CC 67—Suc. 28, (C1428ZAA) Ciudad Autónoma de Buenos Aires, Argentina
[25] Institute of Physics and Astronomy, University of Potsdam, D-14476 Potsdam-Golm, Germany
[26] Department of Physical Sciences, Munster Technological University, Bishopstown, Cork, T12 P928, Ireland
[27] CTAO, Saupfercheckweg 1, D-69117 Heidelberg, Germany
[28] Instituto de Astrofísica de Canarias and Dpto. de Astrofísica, Universidad de La Laguna, E-38200, La Laguna, Tenerife, Spain
[29] Università di Udine and INFN Trieste, I-33100 Udine, Italy
[30] also at International Center for Relativistic Astrophysics (ICRA), Rome, Italy
[31] National Institute for Astrophysics (INAF), I-00136 Rome, Italy
[32] ETH Zürich, CH-8093 Zürich, Switzerland
[33] Institut de Física d'Altes Energies (IFAE), The Barcelona Institute of Science and Technology (BIST), E-08193 Bellaterra (Barcelona), Spain
[34] Japanese MAGIC Group: Institute for Cosmic Ray Research (ICRR), The University of Tokyo, Kashiwa, 277-8582 Chiba, Japan
[35] Technische Universität Dortmund, D-44221 Dortmund, Germany
[36] Croatian MAGIC Group: University of Zagreb, Faculty of Electrical Engineering and Computing (FER), 10000 Zagreb, Croatia
[37] IPARCOS Institute and EMFTEL Department, Universidad Complutense de Madrid, E-28040 Madrid, Spain
[38] Centro Brasileiro de Pesquisas Físicas (CBPF), 22290-180 URCA, Rio de Janeiro (RJ), Brazil
[39] Università di Padova and INFN, I-35131 Padova, Italy
[40] University of Lodz, Faculty of Physics and Applied Informatics, Department of Astrophysics, 90-236 Lodz, Poland
[41] Università di Siena and INFN Pisa, I-53100 Siena, Italy
[42] Deutsches Elektronen-Synchrotron (DESY), D-15738 Zeuthen, Germany
[43] Max-Planck-Institut für Physik, D-80805 München, Germany
[44] Università di Pisa and INFN Pisa, I-56126 Pisa, Italy
[45] Universitat de Barcelona, ICCUB, IEEC-UB, E-08028 Barcelona, Spain
[46] Armenian MAGIC Group: A. Alikhanyan National Science Laboratory, 0036 Yerevan, Armenia
[47] Centro de Investigaciones Energéticas, Medioambientales y Tecnológicas, E-28040 Madrid, Spain
[48] now at Department for Physics and Technology, University of Bergen, NO-5020, Norway
[49] now at University of Innsbruck, Austria
[50] also at Port d'Informació Científica (PIC), E-08193 Bellaterra (Barcelona), Spain
[51] INFN MAGIC Group: INFN Sezione di Torino and Università degli Studi di Torino, I-10125 Torino, Italy
[52] INFN MAGIC Group: INFN Sezione di Bari and Dipartimento Interateneo di Fisica dell'Università e del Politecnico di Bari, I-70125 Bari, Italy
[53] Croatian MAGIC Group: University of Rijeka, Department of Physics, 51000 Rijeka, Croatia
[54] Universität Würzburg, D-97074 Würzburg, Germany
[55] Finnish MAGIC Group: Finnish Centre for Astronomy with ESO, University of Turku, FI-20014 Turku, Finland
[56] now at Ruhr-Universität Bochum, Fakultät für Physik und Astronomie, Astronomisches Institut (AIRUB), D-44801 Bochum, Germany
[57] Departament de Física and CERES-IEEC, Universitat Autònoma de Barcelona, E-08193 Bellaterra, Spain
[58] Japanese MAGIC Group: Physics Program, Graduate School of Advanced Science and Engineering, Hiroshima University, 739-8526 Hiroshima, Japan
[59] Armenian MAGIC Group: ICRAN ET-Armenia at NAS RA, 0019 Yerevan, Armenia
[60] Croatian MAGIC Group: University of Split, Faculty of Electrical Engineering, Mechanical Engineering and Naval Architecture (FESB), 21000 Split, Croatia
[61] now at Department of Astronomy, University of California Berkeley, Berkeley, CA 94720, USA
[62] Croatian MAGIC Group: Josip Juraj Strossmayer University of Osijek, Department of Physics, 31000 Osijek, Croatia

[63] Japanese MAGIC Group: Department of Physics, Kyoto University, 606-8502 Kyoto, Japan
[64] Japanese MAGIC Group: Department of Physics, Tokai University, Hiratsuka, 259-1292 Kanagawa, Japan
[65] also at Dipartimento di Fisica, Università di Trieste, I-34127 Trieste, Italy
[66] Saha Institute of Nuclear Physics, HBNI, 1/AF Bidhannagar, Salt Lake, Sector-1, Kolkata 700064, India
[67] Institute for Nuclear Research and Nuclear Energy, Bulgarian Academy of Sciences, BG-1784 Sofia, Bulgaria
[68] now at Laboratoire d'Annecy de Physique des Particules (LAPP), CNRS-IN2P3, F-74941 Annecy Cedex, France
[69] Japanese MAGIC Group: Department of Physics, Yamagata University, Yamagata 990-8560, Japan
[70] Finnish MAGIC Group: Astronomy Research Unit, University of Oulu, FI-90014 Oulu, Finland
[71] also at INAF Trieste and Dept. of Physics and Astronomy, University of Bologna, Bologna, Italy
[72] Croatian MAGIC Group: Ruder Bošković Institute, 10000 Zagreb, Croatia
[73] INFN MAGIC Group: INFN Sezione di Perugia, I-06123 Perugia, Italy
[74] INFN MAGIC Group: INFN Roma Tor Vergata, I-00133 Roma, Italy
[75] Japanese MAGIC Group: Department of Physics, Konan University, Kobe, Hyogo 658-8501, Japan
[76] University of Namibia, Department of Physics, Private Bag 13301, Windhoek 10005, Namibia
[77] Dublin Institute for Advanced Studies, 31 Fitzwilliam Place, Dublin 2, Ireland
[78] Max-Planck-Institut für Kernphysik, P.O. Box 103980, D-69029 Heidelberg, Germany
[79] High Energy Astrophysics Laboratory, RAU, 123 Hovsep Emin St, Yerevan 0051, Armenia
[80] Aix Marseille Université, CNRS/IN2P3, CPPM, Marseille, France
[81] Centre for Space Research, North-West University, Potchefstroom 2520, South Africa
[82] IRFU, CEA, Université Paris-Saclay, F-91191 Gif-sur-Yvette, France
[83] DESY, D-15738 Zeuthen, Germany
[84] School of Physics, University of the Witwatersrand, 1 Jan Smuts Avenue, Braamfontein, Johannesburg, 2050 South Africa
[85] Department of Physics and Electrical Engineering, Linnaeus University, SE-351 95 Växjö, Sweden
[86] Institut für Astronomie und Astrophysik, Universität Tübingen, Sand 1, D-72076 Tübingen, Germany
[87] Laboratoire Univers et Théories, Observatoire de Paris, Université PSL, CNRS, Université de Paris, 92190 Meudon, France
[88] Sorbonne Université, Université Paris Diderot, Sorbonne Paris Cité, CNRS/IN2P3, Laboratoire de Physique Nucléaire et de Hautes Energies, LPNHE, 4 Place Jussieu, F-75252 Paris, France
[89] Laboratoire d'Annecy de Physique des Particules, Univ. Grenoble Alpes, Univ. Savoie Mont Blanc, CNRS, LAPP, F-74000 Annecy, France
[90] Astronomical Observatory, The University of Warsaw, Al. Ujazdowskie 4, 00-478 Warsaw, Poland
[91] Instytut Fizyki Jądrowej PAN, ul. Radzikowskiego 152, 31-342 Kraków, Poland
[92] University of Oxford, Department of Physics, Denys Wilkinson Building, Keble Road, Oxford OX1 3RH, UK
[93] Université Bordeaux, CNRS/IN2P3, Centre d'Études Nucléaires de Bordeaux Gradignan, F-33175 Gradignan, France
[94] Université de Paris, CNRS, Astroparticule et Cosmologie, F-75013 Paris, France
[95] Institut für Physik und Astronomie, Universität Potsdam, Karl-Liebknecht-Strasse 24/25, D-14476 Potsdam, Germany
[96] Laboratoire Leprince-Ringuet, École Polytechnique, CNRS, Institut Polytechnique de Paris, F-91128 Palaiseau, France
[97] Friedrich-Alexander-Universität Erlangen-Nürnberg, Erlangen Centre for Astroparticle Physics, Erwin-Rommel-Str. 1, D-91058 Erlangen, Germany
[98] Institut für Astro- und Teilchenphysik, Leopold-Franzens-Universität Innsbruck, A-6020 Innsbruck, Austria
[99] Universität Hamburg, Institut für Experimentalphysik, Luruper Chaussee 149, D-22761 Hamburg, Germany
[100] Obserwatorium Astronomiczne, Uniwersytet Jagielloński, ul. Orla 171, 30-244 Kraków, Poland
[101] Landessternwarte, Universität Heidelberg, Königstuhl, D-69117 Heidelberg, Germany
[102] Institute of Astronomy, Faculty of Physics, Astronomy and Informatics, Nicolaus Copernicus University, Grudziadzka 5, 87-100 Torun, Poland
[103] Institut für Physik, Humboldt-Universität zu Berlin, Newtonstr. 15, D-12489 Berlin, Germany
[104] Laboratoire Univers et Particules de Montpellier, Université Montpellier, CNRS/IN2P3, CC 72, Place Eugène Bataillon, F-34095 Montpellier Cedex 5, France
[105] Department of Physics, University of the Free State, PO Box 339, Bloemfontein 9300, South Africa
[106] Nicolaus Copernicus Astronomical Center, Polish Academy of Sciences, ul. Bartycka 18, 00-716 Warsaw, Poland
[107] Department of Physics and Astronomy, The University of Leicester, University Road, Leicester LE1 7RH, UK
[108] GRAPPA, Anton Pannekoek Institute for Astronomy, University of Amsterdam, Science Park 904, 1098 XH Amsterdam, The Netherlands
[109] School of Physical Sciences, University of Adelaide, Adelaide 5005, Australia
[110] Yerevan Physics Institute, 2 Alikhanian Brothers St., 375036 Yerevan, Armenia
[111] Kavli Institute for the Physics and Mathematics of the Universe (WPI), The University of Tokyo Institutes for Advanced Study (UTIAS), The University of Tokyo, 5-1-5 Kashiwa-no-Ha, Kashiwa, Chiba, 277-8583, Japan
[112] Department of Physics, Konan University, 8-9-1 Okamoto, Higashinada, Kobe, Hyogo 658-8501, Japan
[113] RIKEN, 2-1 Hirosawa, Wako, Saitama 351-0198, Japan
[114] Department of Physics, Rikkyo University, 3-34-1 Nishi-Ikebukuro, Toshima-ku, Tokyo 171-8501, Japan
[115] Institute of Space Sciences (ICE, CSIC), Campus UAB, Carrer de Can Magrans s/n, E-08193 Barcelona, Spain
[116] Institut d'Estudis Espacials de Catalunya (IEEC), Gran Capità 2-4, E-08034 Barcelona, Spain
[117] Institució Catalana de Recerca i Estudis Avançats (ICREA), E-08010 Barcelona, Spain
Received 2021 August 6; revised 2021 September 21; accepted 2021 September 22; published 2021 December 24

Abstract

The results of gamma-ray observations of the binary system HESS J0632 + 057 collected during 450 hr over 15 yr, between 2004 and 2019, are presented. Data taken with the atmospheric Cherenkov telescopes H.E.S.S., MAGIC, and VERITAS at energies above 350 GeV were used together with observations at X-ray energies obtained with Swift-XRT, Chandra, XMM-Newton, NuSTAR, and Suzaku. Some of these observations were accompanied by

[118] Corresponding authors: G. Maier gernot.maier@desy.de, D. Hadasch, A. López-Oramas contact.magic@mpp.mpg.de, D. Malyshev, G. Puehlhofer contact.hess@hess-experiment.eu.

Original content from this work may be used under the terms of the Creative Commons Attribution 4.0 licence. Any further distribution of this work must maintain attribution to the author(s) and the title of the work, journal citation and DOI.

measurements of the Hα emission line. A significant detection of the modulation of the very high-energy gamma-ray fluxes with a period of 316.7 ± 4.4 days is reported, consistent with the period of 317.3 ± 0.7 days obtained with a refined analysis of X-ray data. The analysis of data from four orbital cycles with dense observational coverage reveals short-timescale variability, with flux-decay timescales of less than 20 days at very high energies. Flux variations observed over a timescale of several years indicate orbit-to-orbit variability. The analysis confirms the previously reported correlation of X-ray and gamma-ray emission from the system at very high significance, but cannot find any correlation of optical Hα parameters with fluxes at X-ray or gamma-ray energies in simultaneous observations. The key finding is that the emission of HESS J0632 + 057 in the X-ray and gamma-ray energy bands is highly variable on different timescales. The ratio of gamma-ray to X-ray flux shows the equality or even dominance of the gamma-ray energy range. This wealth of new data is interpreted taking into account the insufficient knowledge of the ephemeris of the system, and discussed in the context of results reported on other gamma-ray binary systems.

Unified Astronomy Thesaurus concepts: High energy astrophysics (739); Gamma-ray sources (633); Binary stars (154)

1. Introduction

The most common definition of gamma-ray binaries is based on their composition and their energy output: a gamma-ray binary consists of a compact object orbiting a star, with periodic releases of large amounts of nonthermal emission at energies >1 MeV (Dubus 2013). The class of gamma-ray binary sources consists of fewer than ten members, and every member shows different characteristics. For all of them, except HESS J1832-093 (Martí-Devesa & Reimer 2020), it is known that the massive star is either a Be-type star surrounded by an equatorial circumstellar disk, or an O-type star.

In contrast, the nature of the compact object is unknown for many of the systems. Exceptions are the gamma-ray pulsar binaries PSR B1259-63/LS 2883 and PSR J2032 + 4127/MT91 213, each of which consists of a neutron star and a Be-type star. Pulsations were first discovered in the radio regime for the former one (Johnston et al. 1992) and in the gamma-ray regime for the latter (Abdo et al. 2009). Recently, a transient periodic radio signal in the direction of LS I +61° 303 was claimed (Weng et al. 2021). Together with the magnetar-like flares and the superorbital modulation detected in LS I +61° 303, these are strong hints for a strongly magnetized neutron star in the system (Gregory 2002; Torres et al. 2012; Ackermann et al. 2013). For the binary system HESS J0632 + 057, which also hosts a Be star (MWC 148), the observational characteristics point toward a neutron star as the compact object, interacting with the circumstellar disk of the Be star. Spectroscopic measurements of Hα emission from the Be star indicate a $\leqslant 2.5\,M_{\odot}$ neutron star (Li et al. 2011; Moritani et al. 2018). However, a microquasar scenario, in which particles are accelerated in the jets of a black hole, cannot be ruled out (see Bosch-Ramon & Khangulyan 2009 for a review).

HESS J0632 + 057 was serendipitously discovered as a point-like source at energies above 400 GeV with the H.E.S.S. experiment during a scan of the Monoceros Loop and Rosette Nebula region (Aharonian et al. 2007). This gamma-ray source is coincident with the massive emission-line star MWC 148, which is of spectral type B0pe at a distance of 1.1–1.7 kpc (Morgan et al. 1955; Hinton et al. 2009; Aragona et al. 2010). Associated with this Be star, an X-ray source was detected at soft X-ray energies using XMM-Newton observations, named XMMU J063259.3 + 054801 (Hinton et al. 2009).

The nondetection with the VERITAS experiment (Acciari et al. 2009) provided evidence for variability of HESS J0632 + 057 at gamma-ray energies. HESS J0632 + 057 was later detected again in 2011 February by MAGIC and VERITAS at very high energy (VHE) (Aleksić et al. 2012; Aliu et al. 2014). This detection took place during a high state in X-rays measured with the Neil Gehrels Swift Observatory X-Ray Telescope (Swift-XRT; Falcone et al. 2011). The period of 321 ± 5 days found in X-ray data taken with Swift-XRT established finally the binary nature of HESS J0632 + 057 (Bongiorno et al. 2011). Aliu et al. (2014) later confirmed the periodicity with a larger Swift-XRT data set to be 315^{+6}_{-4} days. HESS J0632 + 057 was detected after 9 yr of accumulating Fermi-LAT data in the orbital phase range 0.0–0.5 (Li et al. 2017) but, because of low statistical significance of the results, the orbital period in the high-energy band could not be determined. The spectral energy distribution (SED) of HESS J0632 + 057 shows two components at high energies, which is typical for gamma-ray binaries (Dubus 2013).

In the radio band, observations were conducted with the Giant Metrewave Radio Telescope (GMRT; 5 GHz) and the Very Large Array (VLA; 1280 GHz; Skilton et al. 2009). They revealed a point-like radio source at the position of MWC 148, at both radio wavelengths, and variability on timescales of roughly one month in the 5 GHz emission. Extended and variable radio emission at 50–100 au scales at 1.6 GHz was discovered by Moldón et al. (2011b) using the European VLBI Network (EVN). They monitored the source over the 2011 January–February X-ray outburst, detecting a shift of the peak of the emission by 21 au over 30 days. Similar behavior has been found in other gamma-ray binaries, such as PSR B1259-63/LS 2883 (Moldón et al. 2011a), LS 5039 (Moldon et al. 2011), or LS I +61° 303 (Massi et al. 2001), which also show a radio morphology with a central core and one-sided extended emission a few au in length.

The actual orbital geometry including eccentricity, position of apastron and periastron, and inclination of the HESS J0632 + 057 binary system is essentially unknown. Two different orbital solutions derived from optical measurements exist with large uncertainties quoted for all relevant parameters. They are derived through different methods and are based on different data sets (see Figure 1). They follow the same definition of phase $\phi = 0$ as MJD = 54,857.0, arbitrarily set to the date of the first Swift-XRT observations (Bongiorno et al. 2011). One solution comes from Casares et al. (2012) using the photospheric absorption lines (mainly He I) of data taken in 2008–2011, and taking the centroid velocity of the Hα emission line to check for the orbital period of the binary (which was fixed to 321 days). The other solution is from Moritani et al. (2018) based on the bisector velocity of the Hα wing, regarding the wavelength where the wing intensity is the same on the blue and red sides as at the center (Shafter et al. 1986) of the Hα emission line from data taken in 2013–2017.

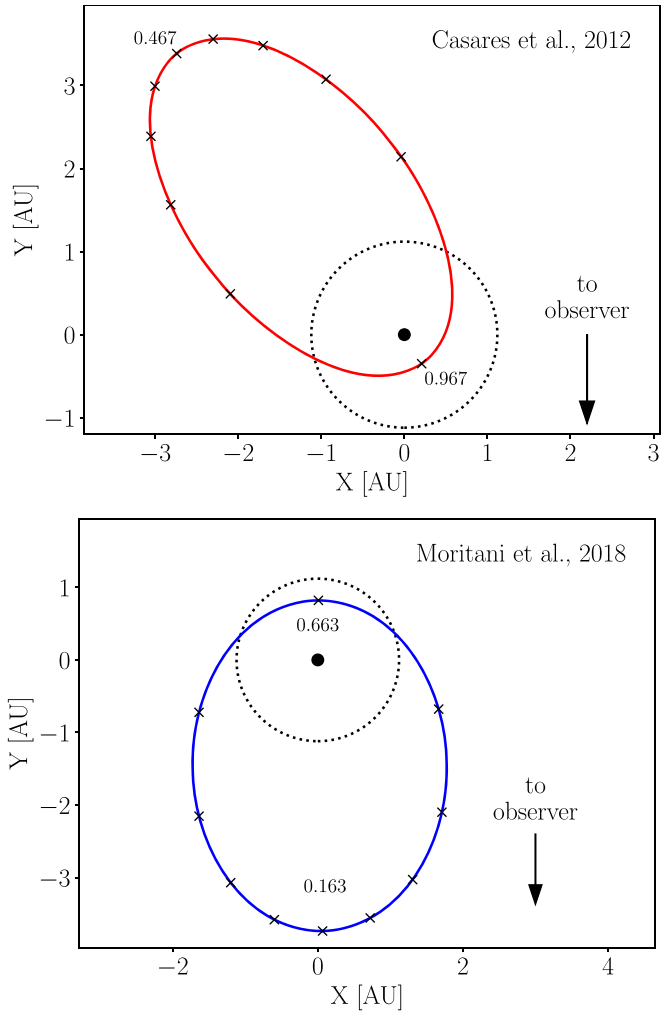

Figure 1. Illustration of the two suggested orbital solutions for HESS J0632 + 057 as seen from above the orbital plane. The very large uncertainties reported for each solution are not shown. Top: orbital solution derived from measurements of photospheric lines of the Be star (Casares et al. 2012). Bottom: orbital solution derived from measurements of the radial velocity of the Hα line (Moritani et al. 2018, Table 1, for $P_{\rm orb} = 313$ days). The massive star is indicated by the black marker. Crosses mark intervals of 0.1 in orbital phase, numbers indicate values for apastron and periastron orbital phase. The dotted line illustrates roughly the size of the disk of the Be star as derived from Hα measurements (Moritani et al. 2015; Zamanov et al. 2016).

The main differences between the two solutions lie in the eccentricity of the orbit and in the orbital phase of periastron passage: $\epsilon \simeq 0.8$ versus $\epsilon \simeq 0.6$ and $\phi = 0.967$ versus $\phi = 0.663$ (Casares et al. 2012; Moritani et al. 2018), respectively. The second significant difference is the prediction of the mass of the compact object as a function of the inclination of the system. The orbital solution provided by Casares et al. (2012) sets an inclination limit of $>60°$ for masses of the compact object consistent with a nonaccreting pulsar. The differences may be due to the different methods applied (absorption versus emission spectra, folding period fixed versus Fourier analysis, epoch of observations, etc.) or due to the sparse data set used by Casares et al. (2012), in which the observations are slightly clustered around periastron.

The Be star in the HESS J0632 + 057 binary, MWC 148, has been studied together with the properties of its disk through optical spectroscopic observations by Moritani et al. (2015) and Zamanov et al. (2016, 2021). Applying the geometry derived by Casares et al. (2012), Zamanov et al. (2016) suggest that the compact object passes deeply into the disk during the periastron passage and that the circumstellar disk is likely truncated by the orbiting compact object. In contrast, Moritani et al. (2015) conclude from the nondetection of variations in Fe II emission lines that the interaction between the compact object and the Be star disk occurs at a distance of two to seven stellar radii from the Be star. Furthermore, they deduced that the detected short-term ($\leqslant$50 days) disk variability is caused by the interaction of the pulsar wind with the disk, rather than by tidal forces.

Optical polarization studies by Yudin et al. (2017) revealed variation in both polarization degree and polarization angle. This finding can be explained by perturbations of the circumstellar material close to periastron passage, applying the orbital solution by Casares et al. (2012), or before and after apastron passage, following the solution of Moritani et al. (2018). However, an additional source of polarized emission, such as a jet, might also explain the changes in polarization (Yudin et al. 2017).

Rea & Torres (2011) performed an X-ray timing and spectral analysis of HESS J0632 + 057 during its high and low states to obtain better insight into the nature of the compact object. No periodic or quasi-periodic signal in any of the emission states was found. Their calculated upper limit on the amplitude of a sinusoidal signal—defined as X-ray pulsed fraction of HESS J0632 + 057—is comparable to limits found for the well-studied binaries LS I +61° 303 and LS 5039. Recently, however, Yoneda et al. (2020) claim to have detected a period of ∼9 s in LS 5039. We caution that the significance after trials is not large for the different observations, that the period detected during different observations varies and requires a high and positive $\dot{P}$, that the orbital corrections do not increase the pulse significance as expected, and that after background subtraction two data sets give rather different pulse fractions. A recent paper by Volkov et al. (2021) finds that the statistical significance of this feature is too low to claim it as a real detection. Comparing the spectral evolution of HESS J0632 + 057 with the TeV binaries LS I +61° 303 and LS 5039 reveals some differences. Specifically, HESS J0632 + 057 shows a steeper X-ray spectrum when the flux is higher, whereas the other two binaries show the opposite behavior. A comparison of the X-ray spectra during the different orbital phases of HESS J0632 + 057 will be discussed later in this paper.

The most recent study of simultaneous observations at hard X-rays with NuSTAR and in TeV gamma-rays with VERITAS was performed by Archer et al. (2020). The data were taken during a period of rising flux. The authors applied a leptonic model, assuming the compact object to be a pulsar, and claim that, under this simple assumption, HESS J0632 + 057 follows the same trend as other binaries: the magnetization of the wind decreases with greater distance from the compact object. According to Archer et al. (2020), this finding strengthens the pulsar scenario for HESS J0632 + 057.

This paper presents results from 15 yr of gamma-ray observations, several years of X-ray observations, and optical observation of HESS J0632 + 057 during different orbital phases. The paper is structured as follows. In Section 2 the instruments used for the studies are described. The results are then presented in Section 3. There the details of the overall light curve, the phase-folded light curves, and the spectra measured during different phases are shown. In Section 3.3 the correlation studies between measurements in the optical (Hα

Table 1
Summary of Gamma-Ray Observations of HESS J0632 + 057

Observatory	Observation Type[a]	Range of Elevations (deg)	Range of Energy Thresholds (GeV)[b]	Observation Time[c] (minutes)	Observation Range (yr)
VERITAS	nominal HV	43–64	160–630	14,995	2008–2019
VERITAS	reduced HV	53–64	420–630	630	2012–2018
H.E.S.S.	CT 1–4	32–62	260–680	7200	2004–2018
MAGIC	Stereo	38–67	147–251	4080	2010–2017

Notes.
[a] VERITAS observations under bright moonlight conditions require different photomultiplier tube camera settings and are labeled with reduced high voltage (HV).
[b] The energy threshold is defined as the lowest energy for events to be used in the analysis. Note that these definitions vary between the observatories, as different spectral reconstruction methods are applied.
[c] Observation time after quality cuts and dead-time correction.

observations), X-ray, and VHE are shown. Subsection 3.4.1 presents the data from the unusual bright outburst from 2018 January. The results are discussed in Section 4 and summarized with final remarks in Section 5.

2. Observations

2.1. H.E.S.S. Gamma-Ray Observations

The H.E.S.S. (High Energy Stereoscopic System) experiment is an array of five imaging atmospheric Cherenkov telescopes located in the Southern Hemisphere in the Khomas Highland of Namibia (23°16′ S, 16°30′ E), at an elevation of 1800 m above sea level. Four telescopes of the array (CT 1–4) have 12 m diameter mirror dishes. A larger, 28 m diameter telescope (CT 5) was deployed at the site in 2012 July during the H.E.S.S. phase-II upgrade.

The telescopes CT 1–4 have been in operation since 2004 (Hinton & the HESS Collaboration 2004) and have a 5° diameter field of view (FoV). CT 5 is equipped with a camera with a 3.5° diameter FoV. Using only CT 1–4, as is done in this work, H.E.S.S. is sensitive to gamma-rays with energies from ∼0.2 TeV up to tens of TeV for observations at zenith.

The H.E.S.S. observations of HESS J0632 + 057 cover almost 14 yr (2004 March–2018 February), totalling 120 h of data after quality cuts, dead-time corrected and taken under dark sky conditions (Table 1). Analysis of 73 h of data obtained prior to 2012 February (MJD 55,951) was reported in Aliu et al. (2014) and these data are reanalyzed in this work, applying improved calibration and reconstruction methods for this paper. All available H.E.S.S. data were processed with the *Image Pixel-wise fit for Atmospheric Cherenkov Telescope* (ImPACT) analysis (Parsons & Hinton 2014) with `std_ImPACT` cut configuration, which requires a minimum of 60 photoelectrons per image.

The signal was extracted from a circular region of radius 0.07° centered on the position of HESS J0632 + 057. For the background estimation, the reflected background method (Fomin et al. 1994; Berge et al. 2007), which ensures that the regions used for signal (ON) and background (OFF) extraction have the same acceptance in the FoV of the camera, was applied. A cross-check of the main analysis was performed using the Model++ analysis (de Naurois & Rolland 2009), yielding compatible results.

2.2. MAGIC Gamma-Ray Observations

The MAGIC (Major Atmospheric Gamma-Ray Imaging Cherenkov Telescopes) experiment is a stereoscopic system of two 17 m diameter imaging atmospheric Cherenkov telescopes. It is located on the Canary Island of La Palma, Spain, at the observatory El Roque de Los Muchachos (28°45′ N, 17°53′ W, 2200 m above sea level). It is equipped with pixelized cameras covering a field of view with a diameter of ∼3°.5. The MAGIC telescopes reach a trigger threshold down to 50 GeV and a sensitivity of ∼ 0.6% of the Crab Nebula flux above 250 GeV in 50 hr of observations at zenith angles <30° (Aleksić et al. 2016).

MAGIC observed HESS J0632 + 057 from 2010 October until 2017 November for a total of 68 hr (Table 1). The data set taken during an X-ray outburst occurring from 2010 October to 2011 March was published in Aleksić et al. (2012). The most recent data cover 2015 December to 2017 November. After quality cuts and correction for dead-time, 57.3 hr of good data remain. These observations were taken both under dark conditions (30.9 hr) and under moderate-to-strong moonlight (26.4 hr). They were carried out in wobble mode, pointing at two regions symmetrically 0.4° away from the source position to simultaneously evaluate the background (Fomin et al. 1994). The data have been analyzed using the standard MAGIC procedure (Zanin et al. 2013). The recorded images were calibrated, cleaned, and parameterized (Hillas 1985; Albert et al. 2008a), while applying different cleaning levels and size cuts for the data in moderate-to-strong moonlight according to Ahnen et al. (2017). The background rejection and the estimation of the gamma-ray arrival direction were performed using the random forest method (Albert et al. 2008b).

2.3. VERITAS Gamma-Ray Observations

The VERITAS (Very Energetic Radiation Imaging Telescope Array System) telescope array is composed of four imaging atmospheric Cherenkov telescopes located at the Fred Lawrence Whipple Observatory in southern Arizona (1268 m above sea level, 31°40′N, 110°57′W; Weekes et al. 2002). Each telescope has a 12 m diameter segmented mirror of $\approx$100 m^2 area. Cherenkov light emitted in extensive air showers is reflected onto photomultiplier cameras covering a field of view of 3°.5 diameter.

The VERITAS observations of HESS J0632 + 057 (VER J0633+057) have been obtained over 11 yr, from 2008 December to 2019 January. For a detailed discussion of the evolution of the performance of the VERITAS instrument with time, see Park & VERITAS Collaboration (2015).

VERITAS observed HESS J0632 + 057 for a total dead-time corrected exposure time of 260 hr, after the application of standard data selection cuts to account for nonoptimal weather or hardware

conditions (see Table 1 for details). HESS J0632 + 057 was observed at an average elevation angle of 60° and at a fixed offset of 0.°5 from the center of the camera's field of view. Observations were taken typically in dark sky conditions, with the exception of a small fraction (∼10 hr) of the data set which was obtained during 30%–65% moonlight. The latter results in a higher energy threshold and reduced sensitivity compared to observations taken under nominal sky conditions (Archambault et al. 2017).

Data were analyzed using VERITAS standard analysis software tools utilizing boosted decision trees for gamma–hadron separation based on image parameters (see, e.g., Krause et al. 2017; Maier & Holder 2017). The source region was defined as a circle with radius 0.°09 around the nominal position of the X-ray source XMMU J063259.3 + 054801. Background event rates are estimated using the reflected background method (Fomin et al. 1994), assuming typically six background regions located symmetrically with respect to the signal region around the camera center. Light-intensity calibration factors obtained from regular monitoring of the optical throughput and of the detector performance are applied to take time-dependent changes in the instrument response into account (Nievas & VERITAS Collaboration 2021). The observations up to 2017 March (MJD 57,822) have been presented before (Aliu et al. 2014; Maier & VERITAS Collaboration 2017). These data have been reanalyzed applying improved calibration and background suppression methods.

2.4. X-Ray Observations

This study includes data obtained with the Swift-XRT, XMM-Newton, Chandra, and NuSTAR instruments. All data presented in Malyshev et al. (2019) were used, adding also Swift-XRT and Chandra data obtained after the publication of the aforementioned paper. Here, only details of analysis for these additional data are provided; for a description of the analysis of NuSTAR and Suzaku data, see Sections 2.4 and 2.5 of Malyshev et al. (2019).

The Swift-XRT data taken between 2018 December 5 and 14 were analyzed with the `heasoft v.6.22` software package and reprocessed with `xrtpipeline v.0.13.4`, as suggested by the Swift-XRT team.[119] The spectra were extracted with `xselect`, using a 36″ circle for source counts and an annulus centered at the source position with inner/outer radii of 60″/300″ for the background. Chandra data were analyzed using `CIAO v.4.9` software and CALDB 4.7.6. The data were reprocessed with the `chandra_repro` utility, source and background spectra with corresponding redistribution matrix files (RMF), and ancillary response files (ARF) were extracted from circular regions of radii 11″ (source) and 50″ (background) with the `specextract` tool. Two Chandra observations (obs. IDs 20974 and 20975; total exposure ∼70 ks) were performed over 2018 February 19–21, about two weeks after the last Chandra observation presented in Malyshev et al. (2019).

For each analyzed X-ray energy spectrum, neighboring energy bins were merged until each bin contained at least one count. Obtained spectra were then fitted in the 0.3–10 keV energy range. The reported fluxes were extracted from the fit of the spectra with an absorbed power-law model (`cflux*phabs*po`) with `XSPEC v.12.9.1m`. The fit was performed with Cash statistics, suitable for the analysis of low-statistics data (Cash 1979).

[119] See the Swift-XRT User's Guide (https://swift.gsfc.nasa.gov/analysis/xrt_swguide_v1_2.pdf).

Table 2
Summary of Hα Profile Measurements of the Be Star MWC 148 in HESS J0632 + 057 using HIDES

Observation Time Range (YYYYMMDD)	Number of Pointings	Total Exposure Time (min)
20131031–20140410	14	2809
20141104–20150402	17	2350
20160107–20160330	6	1020
20161206–20161223	2	443
20170224–20170413	7	1210

2.5. Optical H_α Observations

High-dispersion Hα profiles of the Be star in HESS J0632 + 057 were obtained using the HIDES (High-Dispersion Echelle Spectrograph), a fiber-fed system (Kambe et al. 2013) deployed on a 188 cm telescope at Okayama Astrophysical Observatory (OAO).[120] Furthermore, spectra using ESPaDOnS (Echelle SpectroPolarimetric Device for the Observation of Stars) at the Canada–France–Hawaii Telescope (Manset & Donati 2003) from 2013 October 31 to 2017 April 13 were obtained; see Table 2. The resolving power, R, of HIDES and ESPaDOnS is ∼50,000 and ∼68,000, respectively.

The observations and the data reduction steps are described in detail in Moritani et al. (2018); a short summary is provided here. The HIDES data were reduced using IRAF. The ESPaDOnS data were reduced using the Libre-Esprit/Upena pipeline, provided by the instrument team. The continuum level around the Hα line was refitted and the spectrum was normalized in order to compare with the HIDES data.

The radial velocity was measured as the bisector velocity of the wing of the Hα profile (Moritani et al. 2018) and the FWHM was determined by fitting the middle and bottom of the profiles with a single Gaussian function. The equivalent width (EW) was estimated by simply integrating the profiles. The observations are summarized in Table 2.

3. Results

The gamma-ray observations of HESS J0632 + 057 with H.E.S.S., MAGIC, and VERITAS amount to a large, ∼450 hr data set covering 15 yr, from 2004 to 2019 (see Table 1). The aggregated detection significance over the entire data set, calculated at the position of the X-ray source XMMU J063259.3 + 054801, is 17.9σ for H.E.S.S., 8.9σ for MAGIC, and 27.0σ for VERITAS. Statistical significances are calculated using Equation (17) from Li & Ma (1983). Systematic uncertainties for gamma-ray measurements originate mostly from variations in the atmospheric throughput to Cherenkov photons, mirror reflectivity, camera response, and errors in the background estimations as well as in the efficiencies of signal-selection cuts. The systematic uncertainty is estimated to be 10%–20% on the gamma-ray flux and 0.10–0.15 on the spectral index (Aleksić et al. 2016; Aharonian et al. 2006). Gamma-ray observations are grouped in intervals of approximately 10% of the orbital period due to the generally weak detection significance of individual observations. Shorter periods are used for the flux calculations during high states.

Integral gamma-ray fluxes are calculated throughout this paper above an energy of 350 GeV adopting a gamma-ray

[120] The current Subaru Telescope Okayama Branch Office.

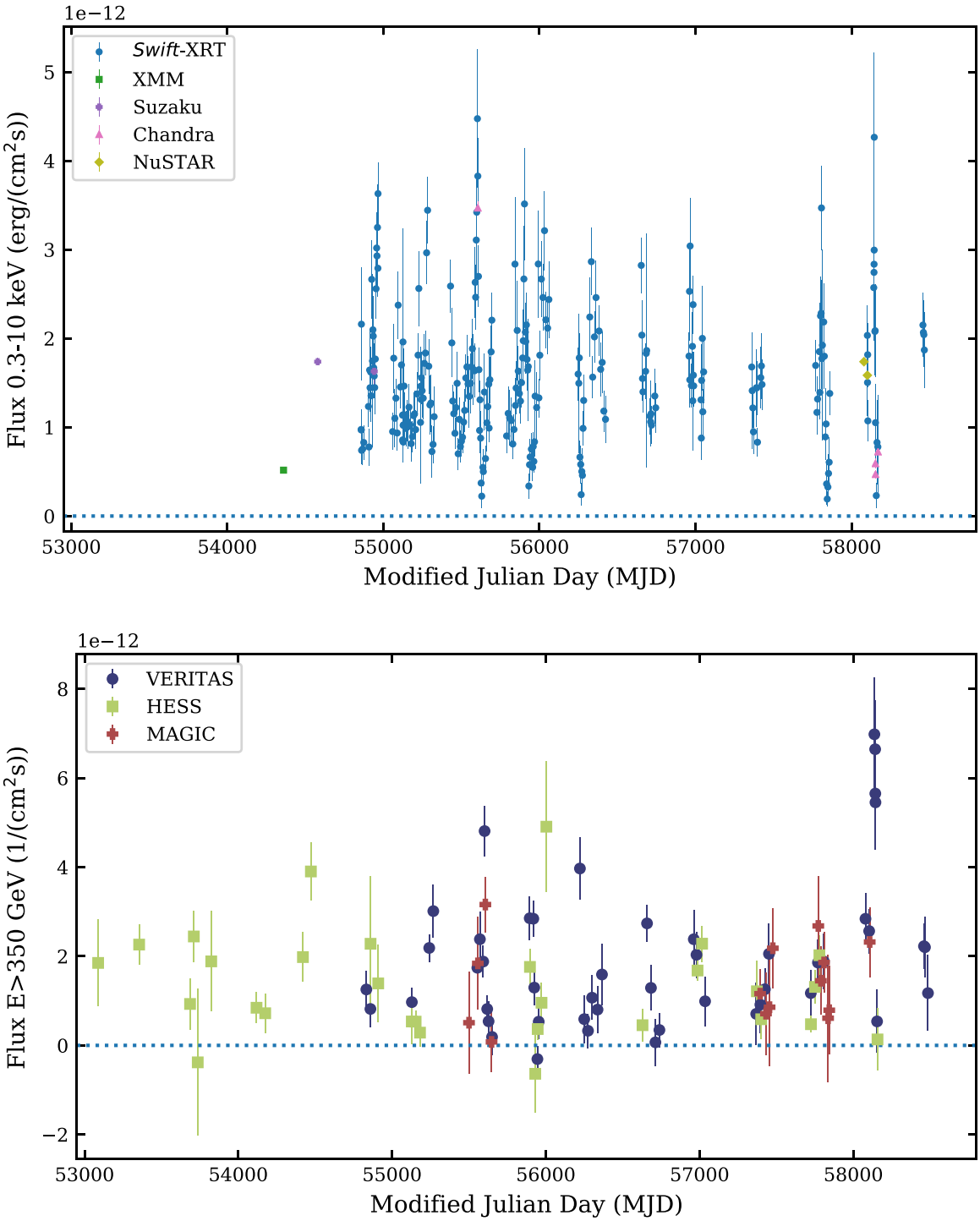

Figure 2. Top: long-term observations of HESS J0632 + 057 in X-rays (0.3–10 keV) with Swift-XRT, XMM-Newton, Suzaku, Chandra, and NuSTAR. Bottom: long-term observations of HESS J0632 + 057 in gamma-rays (>350 GeV) with H.E.S.S., MAGIC, and VERITAS. Vertical lines indicate 68% statistical uncertainties; note that these are smaller than the marker size for all X-ray instruments except Swift-XRT.

spectral index of $\Gamma = 2.6$, which is representative for the data sample (see Table 4 and Section 3.4).

3.1. Light-curve Modulation and Determination of Orbital Period

The long-term light curves (Figure 2) confirm that HESS J0632 + 057 is highly variable at X-ray and gamma-ray energies (see also Acciari et al. 2009; Bongiorno et al. 2011; Aliu et al. 2014). Above 350 GeV, the flux varies between 5% and 10% with respect to the flux of the Crab Nebula (above the same energy), dropping below the detection limits of the different ground-based instruments for some periods.

The large data sets allow us to search for periodic variability patterns on different timescales. The period was first determined to be 321 ± 5 days by Bongiorno et al. (2011) using approximately two years of Swift-XRT measurements (MJD 54,857 to 55,647). Subsequent updates to this analysis, based on extended data sets from Swift-XRT, yielded comparable

Table 3
Results of Derivation of the Orbital Period from Literature in Comparison with the Outcome of This Work

Publication	Energy Range	MJD Range	Method	Orbital Period (days)
Bongiorno et al. (2011)	Swift-XRT	54,857–55,647	Peak fitting	321 ± 5
Aliu et al. (2014)	Swift-XRT	54,857–55,972	ZDCF	315^{+6}_{-4}
Moritani et al. (2018)	Swift-XRT	54,857–57,052	ZDCF	313^{+11}_{-8}
Moritani et al. (2018)	Hα	56,597–57,856	Fourier analysis	308^{+26}_{-23}
Malyshev et al. (2019)	Swift-XRT	54,857–57,860	PCC	$316.2^{+1.8}_{-2.0}$
This work	X-ray	54,857–58,466	PCC	$317.3 \pm 0.7(\text{stat}) \pm 1.5(\text{sys})$
This work	X-ray	54,857–58,466	PDM	$316.7 \pm 1.5(\text{stat}) \pm 1.5(\text{sys})$
This work	X-ray	54,857–58,466	DCF	$318.9 \pm 2.2(\text{stat}) \pm 1.5(\text{sys})$
This work	Gamma-ray	53,087–58,490	PCC	$316.7 \pm 4.4(\text{stat}) \pm 2.5(\text{sys})$
This work	Gamma-ray	53,087–58,490	PDM	$319.0 \pm 3.4(\text{stat}) \pm 2.5(\text{sys})$

Note. The applied methods are: peak fitting (Bongiorno et al. 2011), Z-transformed discrete correlation functions (Alexander 1997, ZDCF), phase dispersion minimization (Stellingwerf 1978, PDM), discrete correlation functions (Edelson & Krolik 1988, DCF), and correlation analysis comparing the light curves with a binned-average light curve (Malyshev et al. 2019, PCC). Errors indicate 1σ statistical uncertainties.

results of $P_{\rm orb} = 313$–321 days (Aliu et al. 2014; Moritani et al. 2018; Malyshev et al. 2019). Flux modulations of the X-ray light curve are interpreted in the literature as being due to the orbital period of the binary system. The only non-X-ray measurement of the orbital period, based on optical observations of Hα radial velocity profiles, yielded $P_{\rm orb} = 308^{+26}_{-23}$ days (Moritani et al. 2018), again compatible with previous results (see Table 3 for a summary of the measurements of orbital period). Although Casares et al. (2012) did not estimate the orbital period, they showed that the main parameters of the Hα emission line (equivalent width, FWHM, and centroid velocity) are modulated within the 321 day X-ray period and calculated an orbital solution of the binary.

The analysis of the most recent available Swift-XRT data set including the reanalysis of older data (264 data points for MJD 54,857–58,466; see Figure 2, top), considered in this study using a method based on Pearson's correlation coefficient (PCC method; see Appendix A), results in an orbital period of $P_{\rm orb} = 317.3 \pm 0.7(\text{stat}) \pm 1.5(\text{sys})$ days (see Table 3). Systematic uncertainties are derived from the application of the different methods for the period derivation applied to 1000 Monte Carlo (MC)-generated data sets. The description of the application of additional methods, such as discrete correlation functions (DCF) or phase dispersion minimization (PDM), together with details of the analysis of the period and derivation of the associated systematic uncertainties, can be found in Appendix A. Periodic signals on timescales different from the orbital period have been observed in high-mass X-ray binaries, e.g., the superorbital period of 1667 days detected in radio, optical, X-ray and gamma-ray observations of the binary LS I +61° 303 (Gregory 2002; Li et al. 2011; Ackermann et al. 2013; Paredes-Fortuny et al. 2015b; Ahnen et al. 2016; Kravtsov et al. 2020). A signal at periods other than the orbital period has not been found for periods between 50 and 1000 days in an analysis of the X-ray observations of HESS J0632 + 057 using the PCC method (see Appendix A and Figure 12(d)). The analysis of MC-generated light curves with similar time structures shows that the PCC periodogram obtained from the analysis of the measured light curve is consistent with expectations from statistical fluctuations.

The large gamma-ray data set, spanning almost 15 yr of gamma-ray observations (Figure 2, bottom), allows the orbital period of this system to be determined from gamma-ray data alone for the first time. The approach of the analysis is equivalent to that of the X-ray analysis discussed above (PCC method), resulting in an orbital period $P_\gamma = 316.7 \pm 4.4(\text{stat}) \pm 2.5(\text{sys})$ days, consistent with the value obtained at X-ray energies (see again Appendix A for details on the analysis). Given the known strong correlation of X-ray and VHE gamma-ray fluxes observed in the past (Aliu et al. 2014, see also Subsection 3.3), this result is not unexpected.

Table 3 summarizes the outcome of the different analyses of orbital period in comparison with results from the literature. For period-folding, the result from the PCC method was used in this paper. It was applied to the Swift-XRT data with the following values: $\text{MJD}_0 = 54{,}857$ (arbitrarily set to the date of the first observations of the source with Swift) and period $P = 317.3 \pm 0.7$ (stat) $\pm$ 1.5(sys) days. It should be stressed that none of the conclusions on the physical properties of the binary system depend on this particular choice (see also Appendix B and Figures 13 and 14).

3.2. Phase-folded Light Curves

The light curves at X-ray and gamma-ray energies were both folded with the adopted orbital period of 317.3 days using $\phi = 0$ as MJD=54,857.0, arbitrarily set to the date of the first Swift-XRT observations (Bongiorno et al. 2011). These folded light curves reveal several prominent features (see Figure 3): a maximum around phases 0.2–0.4, a minimum at phases 0.4–0.6, a second (lower) peak around phases 0.6–0.8, and a broader plateau around 0.8–0.2. HESS J0632 + 057 is now detected at energies >350 GeV with high statistical significance at all orbital phases with the exception of the region around the first minimum, at phases 0.4–0.6 (Table 4). According to the orbital solution of Casares et al. (2012), the periastron is located at phase $\phi = 0.967$, coincident with the gamma- and X-ray flux plateau, while apastron takes place during the dip/minimum, at phase $\phi = 0.467$. For the orbital solution proposed by Moritani et al. (2018), periastron takes place at $\phi = 0.663$, during the second peak, while apastron happens at $\phi = 0.163$ (see Figure 1 for a representation of the suggested solutions). The phase-folded parameters of the Hα measurement results are shown in Figure 4. No significant modulation is seen in EW, whereas the radial velocity and FWHM show small variations as a function of orbital phase. Note that Moritani et al. (2018) proposed an orbital solution using the radial velocity of Hα.

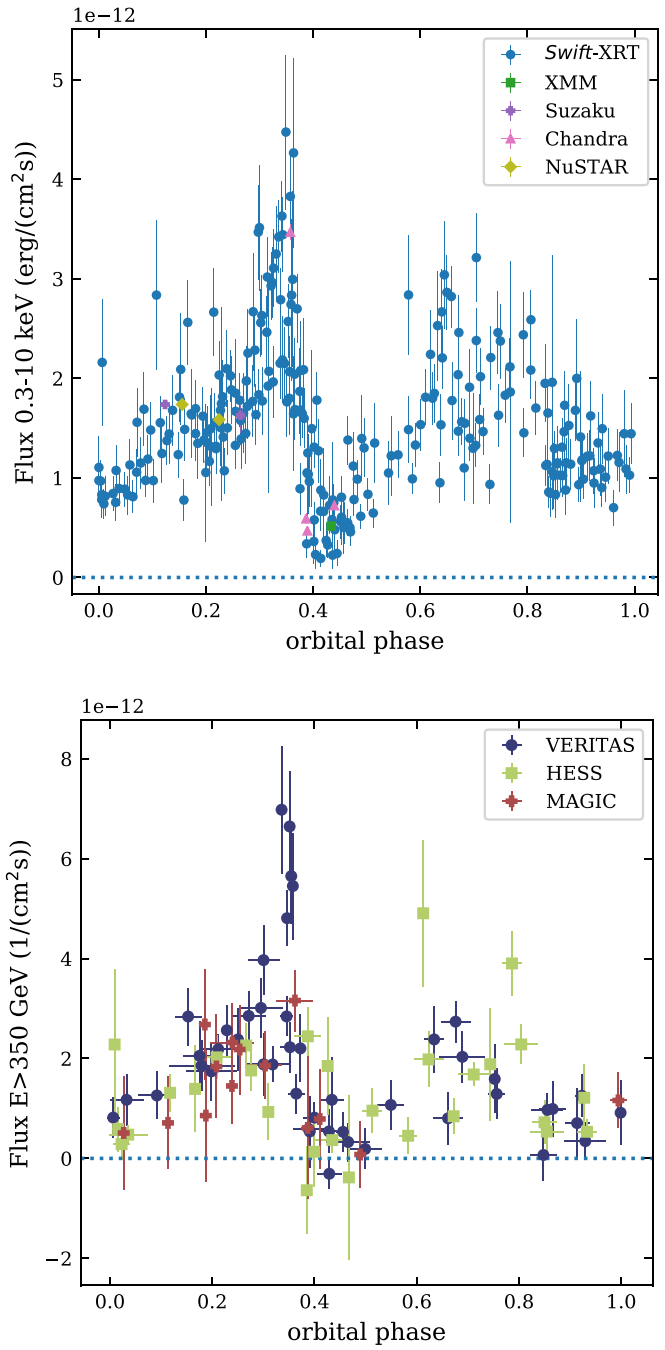

Figure 3. X-ray (0.3–10 keV; top) and gamma-ray (>350 GeV; bottom) light curves as a function of the orbital phase, assuming an orbital period of 317.3 days ($MJD_0 = 54{,}857.0$; Bongiorno et al. 2011). Vertical error bars indicate statistical uncertainties; note that these are smaller than the marker size for all X-ray instruments except for Swift-XRT. Fluxes are averaged over time intervals indicated by the horizontal lines (for most flux points these are smaller than the marker size).

HESS J0632 + 057 has been observed over 14 orbits at X-ray and 18 orbits at gamma-ray energies (see Appendix C and especially Figures 15 and 16). Despite more than 270 X-ray pointings and ∼450 hr of gamma-ray observations, these data cover most orbits relatively sparsely. Only five orbits (orbits 7–11 in Figure 15) have been regularly monitored at X-ray energies over more than 50% of an individual orbit. Ground-based gamma-ray instruments covered an even smaller range, as they cannot observe the binary for a large fraction of its orbit due to visibility constraints. Four orbits have been observed in the phase range 0.2–0.4 with notable coverage in X-ray and gamma-ray observations (Figure 9) and are discussed in more detail in Section 3.4.1.

3.3. Correlation Analysis

Correlations between X-ray and gamma-ray flux measurements are shown in Figure 5 (top). Gamma-ray observations are averaged over several nights in order to achieve sufficient statistical detection significance, while X-ray observations are nightly averages. Measurements are considered to be contemporaneous in this context for X-ray observations taking place during the time period of the grouped gamma-ray observations (the maximum interval length for the grouped gamma-ray observations is ∼10% of the orbital period). Average X-ray fluxes are used for periods of gamma-ray observations including several X-ray data points. It is worth stating that both the X-ray and gamma-ray fluxes are measured to be variable on timescales as short as hours, and the total X-ray exposure associated with each point is typically just a small fraction of the gamma-ray exposure. This might contribute to some of the scattering between fluxes in both energy bands as observed in Figure 5 (top). The DCF method (Edelson & Krolik 1988) is used to quantify the correlation and to search for possible time lags between X-ray and gamma-ray emission patterns. Figure 5 (bottom) shows the DCF using a binning of 5 days (different binnings have been tried with no significant changes in the results) and with confidence limits calculated using the toy Monte Carlo technique as recommended in Uttley et al. (2003). The correlation coefficient is 0.82 at time lag $\tau = 0$ and the p-value for noncorrelation is 4×10^{-15}, calculated from 59 flux pairs. The ratio of gamma-ray (>350 GeV) to X-ray flux (0.3–10 keV) is on average 2.9 ± 0.3, estimated from a linear fit as shown in Figure 5 (top) for the chosen integration ranges in energy. This underlines the equality or even dominance of the gamma-ray energy range for the emission of the binary system with respect to the X-ray regime (see also Figure 8). The fit also indicates a nonzero X-ray flux ($F_{0.3-10\,\mathrm{keV}} = (6.1 \pm 1.5) \times 10^{-13}$ erg cm^{-2} s^{-1}) for a vanishing gamma-ray component, suggesting an X-ray source partially unrelated to the gamma-ray emission. No indication of a significant time lag between X-ray and gamma-ray emission is observed (see Figure 5, bottom), although this measurement is not sensitive to time lags $\tau \lessapprox 10$ days due to the required grouping of the gamma-ray observations. In general, this confirms the strong correlation between gamma-ray and X-ray emission, as already shown in Aliu et al. (2014). Ranked and unranked correlation analyses result in similar correlation coefficients between 0.75 and 0.82. This points toward a close-to-linear correlation, although statistical uncertainties of the photon fluxes observed in both energy bands prevent us from making any strong statements regarding possible nonlinearities between gamma-ray and X-ray emission.

No correlation is found between any parameters obtained from the optical Hα measurements and X-ray or gamma-ray fluxes (Figure 6). The Spearman correlation coefficients are between –0.4 and 0.33 for time lags $\tau = 0$, corresponding to p-values for noncorrelation between 0.02 and 0.85 (calculated from 18 gamma-ray/Hα and 31 X-ray/Hα pairs). A relaxed definition for contemporaneous data is used for the Hα correlation analysis with a time span of ±5 days, well below the shortest timescales of ≈50 days observed for Hα profile

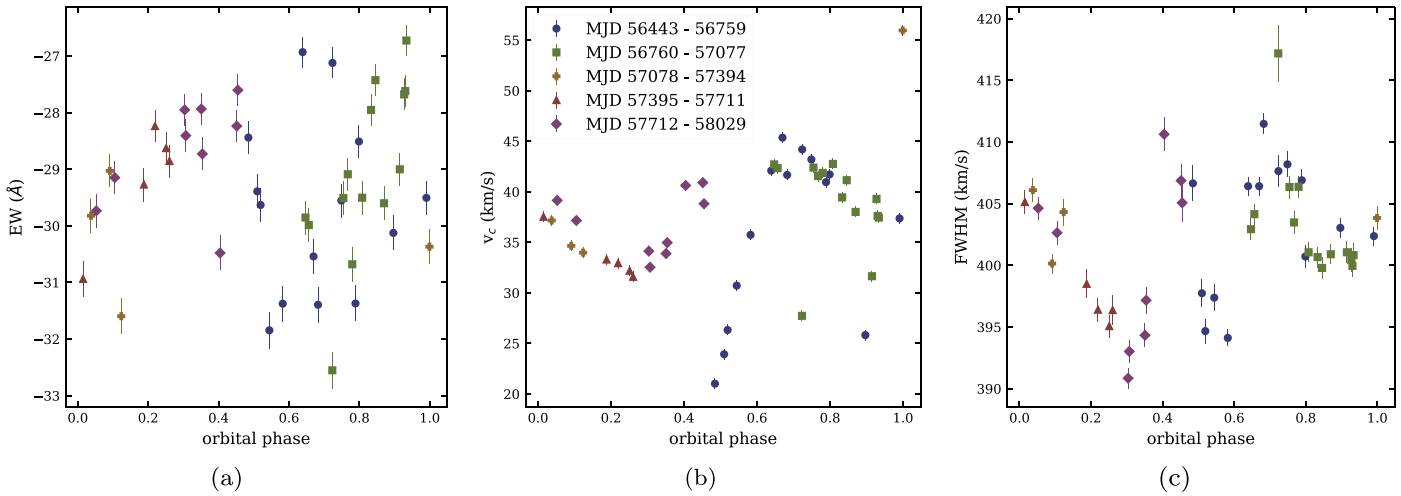

Figure 4. Results from Hα measurements of MWC 148 vs. orbital phase, assuming an orbital period of 317.3 days. Different markers indicate individual orbits, as indicated by the intervals in MJD in the figure legend in the central panel. (a) Hα equivalent width (EW); (b) Hα radial velocity; (c) Hα FWHM. See Section 2.5 for definitions of EW and FWHM.

Table 4
Summary of Observations and Spectral Analyses at Gamma-Ray Energies Averaged over Different Ranges in Orbital Phase Assuming an Orbital Period of 317.3 days

Observatory	Exposure (hr)	Significance[a] (σ) (pre-trial)	Flux Normalization Constant at 0.5 TeV[b] [cm^{-2} s^{-1} TeV^{-1}]	Photon Index	Cutoff Energy [TeV]	χ^2/N[c]
Orbital phase range 0.2–0.4 (high state)						
VERITAS	119.3	25.5	$(45.6 \pm 2.4) \times 10^{-13}$	2.67 ± 0.04	⋯	45.17/7
VERITAS (epl)			$(57.2 \pm 4.2) \times 10^{-13}$	1.79 ± 0.16	1.75 ± 0.38	4.5/6
H.E.S.S.	17.3	9.9	$(34.0 \pm 4.4) \times 10^{-13}$	2.45 ± 0.12	⋯	4.6/7
MAGIC	35.5	9.6	$(34.8 \pm 4.6) \times 10^{-13}$	2.48 ± 0.11	⋯	13.5/8
Orbital phase range 0.4–0.6 (low state)						
VERITAS	40.0	2.4	⋯	⋯	⋯	⋯
H.E.S.S.	18.7	2.9	⋯	⋯	⋯	⋯
MAGIC	5.2	0.6	⋯	⋯	⋯	⋯
Orbital phase range 0.6–0.8 (high state)						
VERITAS	28.4	11.0	$(31.6 \pm 3.9) \times 10^{-13}$	2.52 ± 0.14	⋯	3.3/6
H.E.S.S.	30.4	13.8	$(32.0 \pm 3.5) \times 10^{-13}$	2.34 ± 0.1	⋯	15.25/15
MAGIC	—	⋯	⋯	⋯	⋯	⋯
Orbital phase range 0.8–0.2						
VERITAS	72.7	8.9	$(20.8 \pm 3.1) \times 10^{-13}$	2.67 ± 0.17	⋯	3.2/4
H.E.S.S.	53.6	8.3	$(16.2 \pm 2.6) \times 10^{-13}$	2.55 ± 0.15	⋯	5.3/2
MAGIC	27.4	3.4	⋯	⋯	⋯	⋯

Notes. The table lists the results of the power-law fits ($dN/dE = N_0(E/0.5\ \mathrm{TeV})^{-\Gamma}$) to the differential energy spectra obtained separately for H.E.S.S., MAGIC, and VERITAS. For one measurement, the result of a fit using a power law with exponential cutoff ($dN/dE = N_0(E/0.5\ \mathrm{TeV})^{-\Gamma}e^{-E/E_c}$; marked as epl) is listed. Errors are 1σ statistical errors only. The systematic errors are 11%–20% on the flux constant and 0.10–0.15 on the spectral index.
[a] Significances are calculated following the maximum likelihood ratio test method proposed in Li & Ma (1983).
[b] Flux normalization constants are calculated for all data sets for easier comparison at the same energy (0.5 TeV) and not at the decorrelation energy.
[c] N comes from number of spectral bins in estimated energy used to fit the data. The spectrum itself is obtained via forward folding to those bins.

variability (Moritani et al. 2015). This relaxation of the contemporaneity criteria is necessary to obtain a reasonable number of pairs of observations, but might obscure variability on shorter timescales. The low gamma-ray fluxes and large uncertainties might hide possible correlations. It should also be noted that the optical Hα data were obtained during five orbital periods (MJD 56,597–57,857; orbits 12–16 in Figures 15 and 16) with generally sparse coverage of X-ray and gamma-ray observations. This results in no contemporaneous observation pairs at TeV/Hα around orbital phases 0.3–0.6, which correspond to the first maximum and the dip in the folded light curve. In the case of the contemporaneous observation pairs at X-ray/Hα, there is no coverage at orbital phases 0.0–0.2 and 0.5–0.6. This imperfect coverage of orbital phases might also obscure possible correlations.

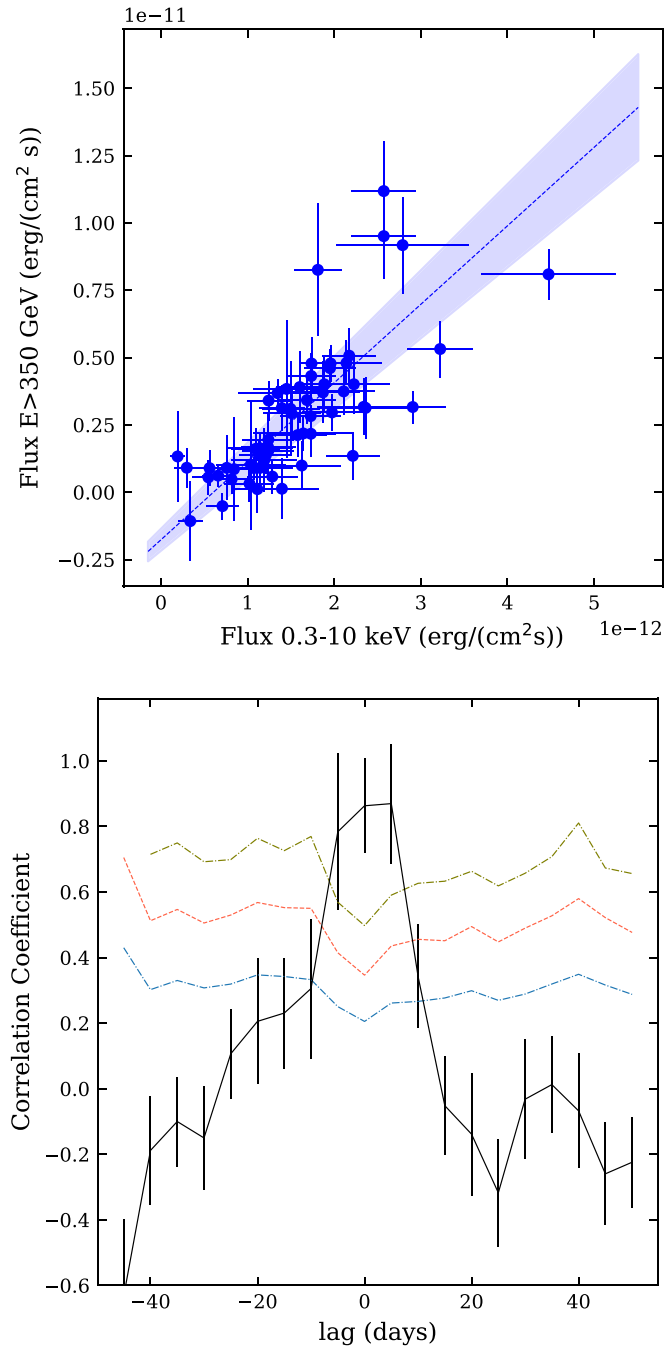

Figure 5. Top: contemporaneous gamma-ray (>350 GeV) vs. X-ray (0.3–10 keV) integral fluxes. In total, 59 measurements were selected with X-ray measurements taking place during the period of gamma-ray observations. The dashed line and shaded area indicate the results of a linear fit to the data and the 1σ error range, respectively. Bottom: discrete cross-correlation function (DCF) between gamma-ray and X-ray data assuming a bin width for the time lag $\Delta\tau = 5$ days. The dashed lines indicate the 2σ, 3σ, and 4σ confidence levels (from bottom to top) derived from 100,000 toy Monte Carlo light curves. Only correlation coefficients with time lags consistent with zero are significant.

3.4. Flux States and Spectral Analysis

The data sets are divided into four different bins in orbital phase for the spectral analysis: the two higher flux states with orbital phases 0.2–0.4 and 0.6–0.8, the low state at orbital phases 0.4–0.6, and the medium (plateau) state for the remaining phases 0.8–0.2. This approach ignores the variability of the source on timescales shorter than these bins, as well as possible orbit-to-orbit variability, but allows a sufficient number of excess events to be collected for high-statistics spectra.

Results from the spectral analysis are summarized in Figure 7 and Table 4. The differential gamma-ray energy spectra in the four phase ranges are consistent within statistical uncertainties with simple power laws $dN/dE = N_0(E/(0.5\ \mathrm{TeV}))^{-\Gamma}$ with the exception of the long-exposure data set obtained with VERITAS for phase bin 0.2–0.4. Here, a spectral fit assuming a power law with exponential cutoff $(dN/dE = N_0(E/(0.5\ \mathrm{TeV}))^{-\Gamma}e^{-E/E_c})$ with $E_c = 1.75 \pm 0.38$ TeV provides a significantly better reduced χ^2 than a power-law fit without cutoff. Shorter exposure times at other phase bins of H.E.S.S. and MAGIC observations prevent us from measuring or refuting similar changes in the spectral shapes with those data sets. All measurements of the differential energy spectra by H.E.S.S., MAGIC, and VERITAS are compatible, within statistical and systematic uncertainties. No variability of the spectral index Γ is observed among spectra in different orbital phase bins, considering the statistical uncertainties. The spectral energy distributions for the four different phase bins are shown in Figure 8, including the X-ray spectra, which have been obtained in the same way by averaging over the phase bins discussed above. HESS J0632 + 057 is only weakly detected in the energy range covered by the Fermi-LAT, therefore only a phase-averaged spectrum is shown, taken from Li et al. (2017).

3.4.1. Detailed Examination of Orbits 9, 10, 16, and 17

Four orbits in the data sets presented provide reasonably good X-ray and gamma-ray coverage around orbital phase values of 0.2–0.45, which includes the first maximum and subsequent flux decay. Figure 9 shows the light curves for the four orbits with gamma-ray and X-ray coverage: 9, 10, 16, and 17. The shapes of the light curves of these four orbits differ notably and suggest the existence of orbit-to-orbit variability. The short-timescale variability on timescales of 20 days and less has been seen at X-ray energies (see also Figure 2). The observed differences in fluxes between orbits might be a biased view due to observations taking place at slightly different orbital phases. Observations during orbits 9 (2011 Jan) and 17 (2018 Jan) reveal gamma-ray and X-ray emission in bright states, comparable to the highest ever observed from this binary. The X-ray flux in orbits 10 and 16 is a factor of ∼1.5 lower than in orbits 9 and 17 at orbital phases of 0.35. The maximum gamma-ray flux also appears to be lower, although the low cadence of observations in this energy range does not allow a firm statement to be made.

The bright state in orbit 9 has been reported in previous work by the MAGIC and VERITAS collaborations (Aleksić et al. 2012; Aliu et al. 2014). The gamma-ray flux for orbit 17 reached a level of $(7.0 \pm 1.3) \times 10^{-12}$ photons cm^{-2} s^{-1} above 350 GeV (corresponding to ≈7% of the flux of the Crab Nebula above the same energy). In this same orbit, HESS J0632 + 057 was detected on three individual nights within one week of observations with $>7\sigma$ statistical significance per night (see Table 5).

The determination of variability timescales is limited by the cadence of the observations. For orbit 17, the flux changes from the highest state on MJD 58,136 to a flux below the detection limit on MJD 58,153 (flux upper limit for MJD 58,153: $F_{99\%\mathrm{CL}}(>350\ \mathrm{GeV}) < 2.6 \times 10^{-12}$ photons cm^{-2} s^{-1}), indicating a flux decay time shorter than 17 days. A similar timescale

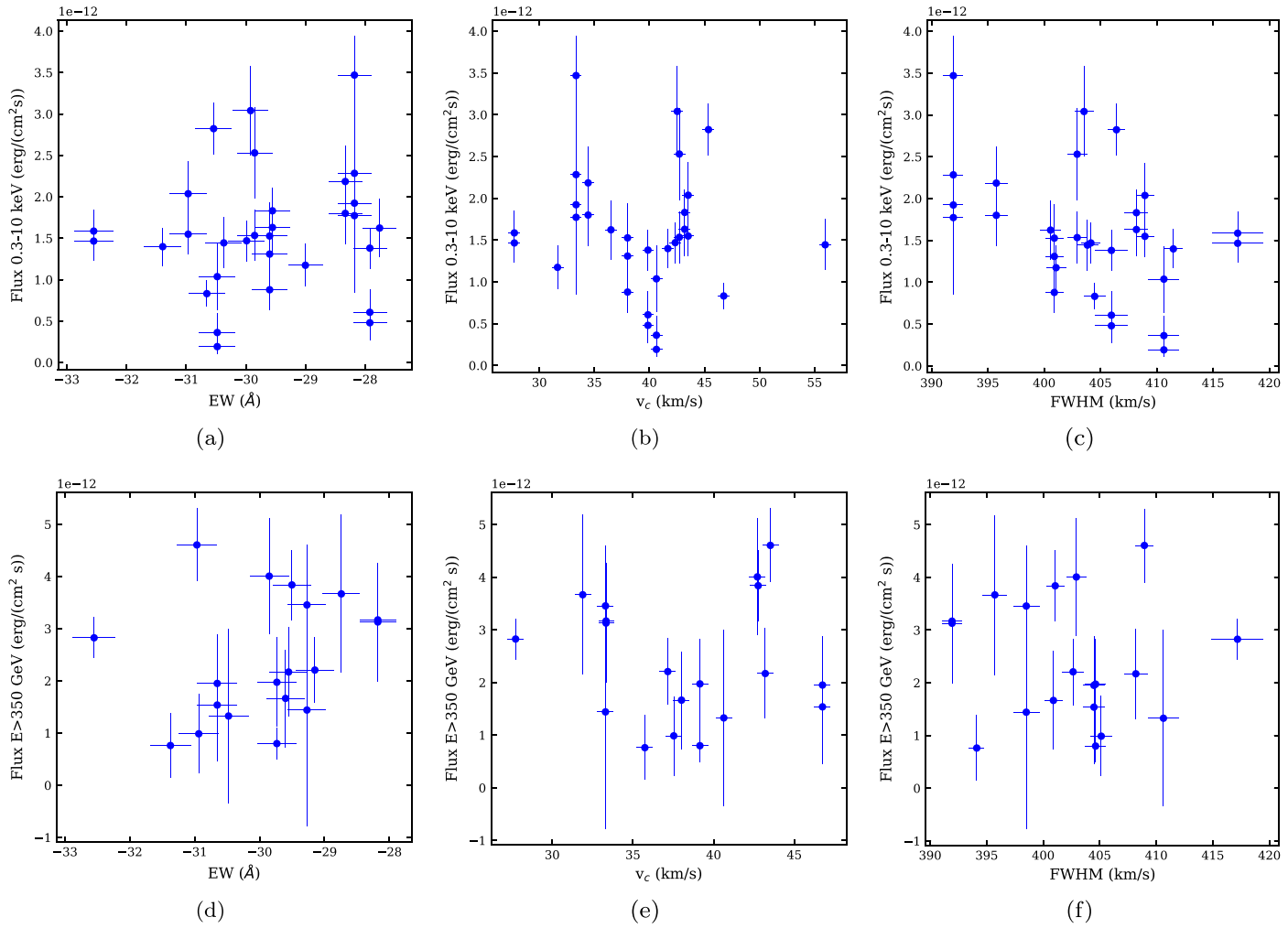

Figure 6. Hα measurements of MWC 148 vs. X-ray (top; panels (a)–(c)) and gamma-ray (bottom; panels (d)–(f)) measurements. In total 31 (19) measurements were selected with a maximal difference of observation dates of 5 days for the X-ray/Hα (gamma-ray/Hα) correlation analysis.

of roughly 20 days or less, again limited by the cadence and detection statistics of the observations, is observed for orbit 9.

The spectral energy distributions for orbits 9 and 17 are shown in Figure 10 and results for spectral fits to the gamma-ray data, assuming power-law functions, are given in Table 5. Despite the dramatic changes of the overall flux levels, no evidence for variability of the spectral index is detected, within statistical errors, for all six periods of gamma-ray observations.

4. Discussion

4.1. VHE Results and Acceleration Mechanisms

HESS J0632 + 057 has been observed at VHE with irregular coverage across 18 orbits, spanning an observational period from 2004 to 2019. These observations result in a statistically significant detection of nonthermal emission at all orbital phases, except phases 0.4–0.6. The phase-averaged luminosity of HESS J0632 + 057 above 1 TeV is $\approx 10^{32}$ erg s^{-1} (assuming a distance of 1.4 kpc), making it one of the faintest gamma-ray binaries known to date (see Dubus 2013). The VHE gamma-ray emission extends beyond several TeV (see Figure 7), indicating the existence of radiating particles with at least similar energies. The energy range for the detected emission and the spectral shapes of individual spectra are, within statistical uncertainties, independent of the orbital phase of the measurement. The spectra follow approximately power-law shapes with spectral indices in the range 2.3–2.6 (Table 4), in line with generic expectations from diffusive shock acceleration.

In general, and independent of the nature of the compact object (black hole or neutron star), the VHE emission can be produced through interactions of accelerated hadrons or leptons with surrounding matter, magnetic, or radiation fields. The literature (e.g., Khangulyan et al. 2007) provides detailed discussions of mechanisms for acceleration and losses (e.g., synchrotron radiation, anisotropic inverse Compton scattering, or adiabatic losses) as functions of density and magnetic field strengths in binary systems. The discussion of the nonthermal processes at work in HESS J0632 + 057, including particle acceleration and X- and gamma-ray emission and absorption processes, is limited by the uncertainties present in some of the fundamental characteristics of the system. In particular, the unknown nature of the compact object allows different scenarios for the required power source for particle acceleration to be considered (e.g., the interaction of the stellar wind with an accretion-driven relativistic jet or with a pulsar wind). Equally important are the difficulties in determining the orbital geometry, given that two discrepant solutions with large uncertainties are found in the literature (Figure 1). Further uncertainties include the size and orientation of the equatorial

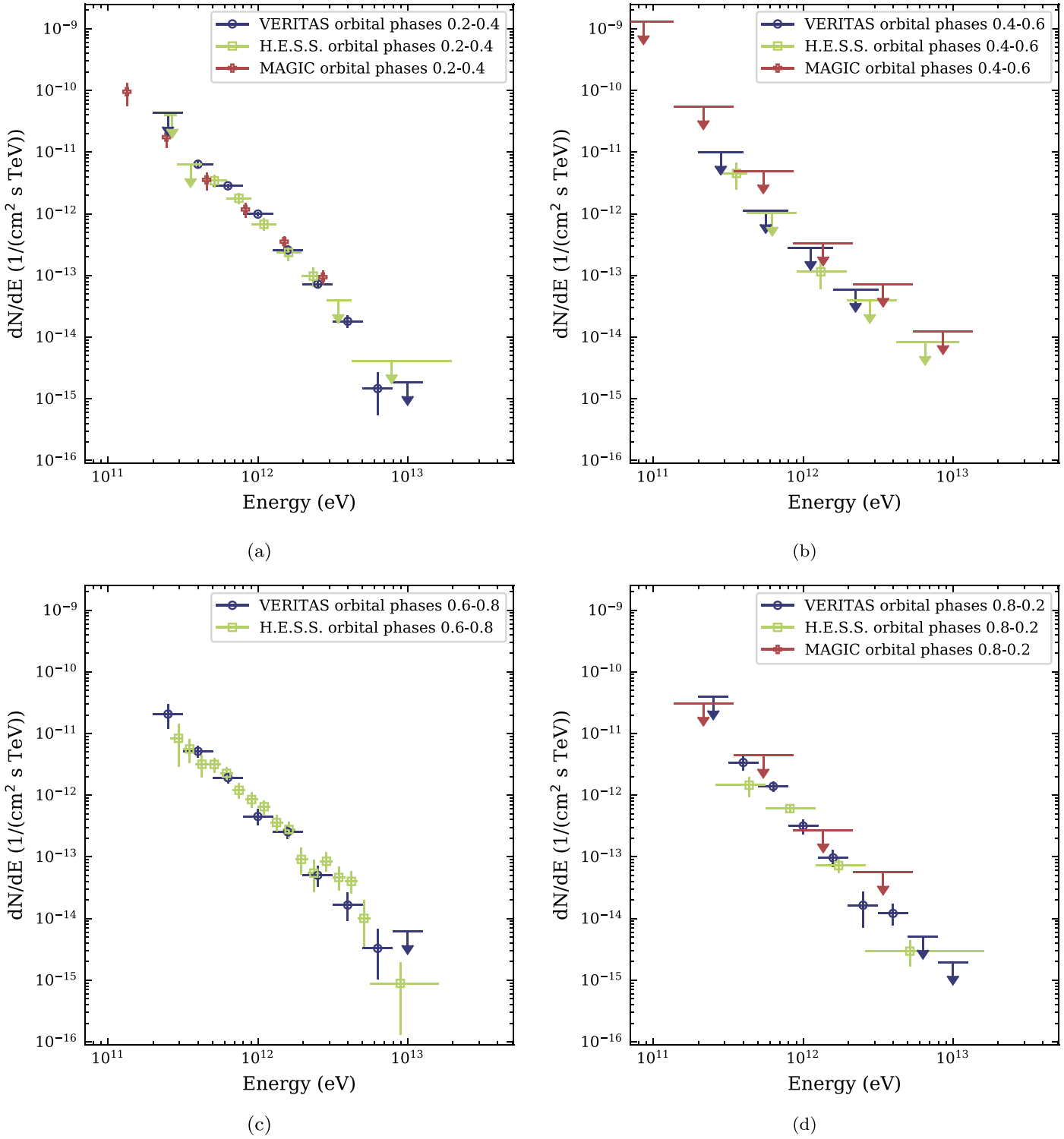

Figure 7. Differential energy spectra of photons above 200 GeV obtained by H.E.S.S., MAGIC, and VERITAS averaged over all available orbits. The figure shows the results for four different orbital phase bins: (a) orbital phases 0.2–0.4; (b) orbital phases 0.4–0.6; (c) orbital phases 0.6–0.8; (d) orbital phases 0.8–0.2. Vertical error bars show 1σ uncertainties; downward pointing arrows indicate upper limits at the 95% confidence level.

disk of the Be star, the mass-loss rates and velocities of both equatorial and isotropic stellar winds, the properties of the accreting object (in the case of a black hole) or the pulsar wind (in the case of a neutron star), and the magnetic field configuration in the acceleration region.

4.2. Flux Variability Studies

The 15 yr of H.E.S.S., MAGIC, and VERITAS observations of HESS J0632 + 057, combined with measurements at optical and X-ray energies, suggest multiple patterns of variability on different timescales in the binary system. The most prominent

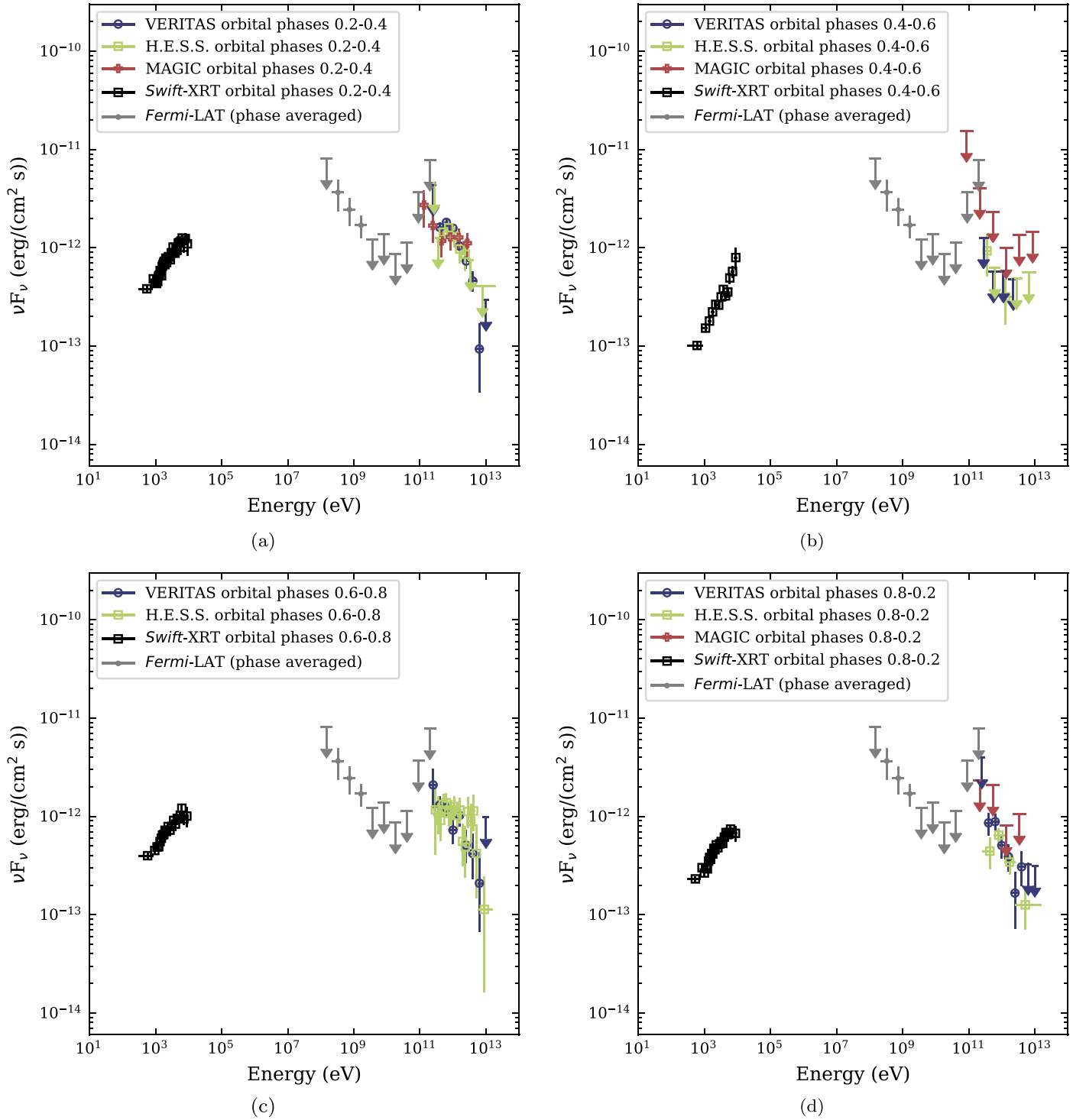

Figure 8. Spectral energy distribution for HESS J0632 + 057 averaged over all available orbits. The figure shows the result for four different phase bins: (a) orbital phases 0.2–0.4; (b) orbital phases 0.4–0.6; (c) orbital phases 0.6–0.8; (d) orbital phases 0.8–0.2. Downward pointing arrows indicate upper limits at the 95% confidence level. Gray points show the phase-averaged spectrum measured by the Fermi-LAT (Li et al. 2017).

modulation, interpreted as the orbital period, is consistently seen, within statistical uncertainties, in X-ray and gamma-ray measurements (P_X =317.3 ± 0.7(stat) ± 1.5(sys); P_γ = 316.7 ± 4.4(stat) ± 2.5(sys), see Section 3.1). In both bands, the orbital-phase-folded light curves (Figure 3) show two maxima at phases $\Phi \approx 0.3$ and $\Phi \approx 0.6$–0.8, separated by a deep flux minimum at orbital phase $\Phi \approx 0.4$. In the VHE band, the first maximum is more pronounced and exhibits, at least for some orbits, a sharp peak with a duration of a few days. The locations of the extrema in the X-ray and gamma-ray light curves along the binary orbit are not known, due to the large uncertainties in the orbital solutions, as discussed above. Assuming orbital parameters as presented in Casares et al. (2012) (Figure 1, top), the first maximum and the second maximum occur before and after apastron, where the environment around the compact object could likely be the

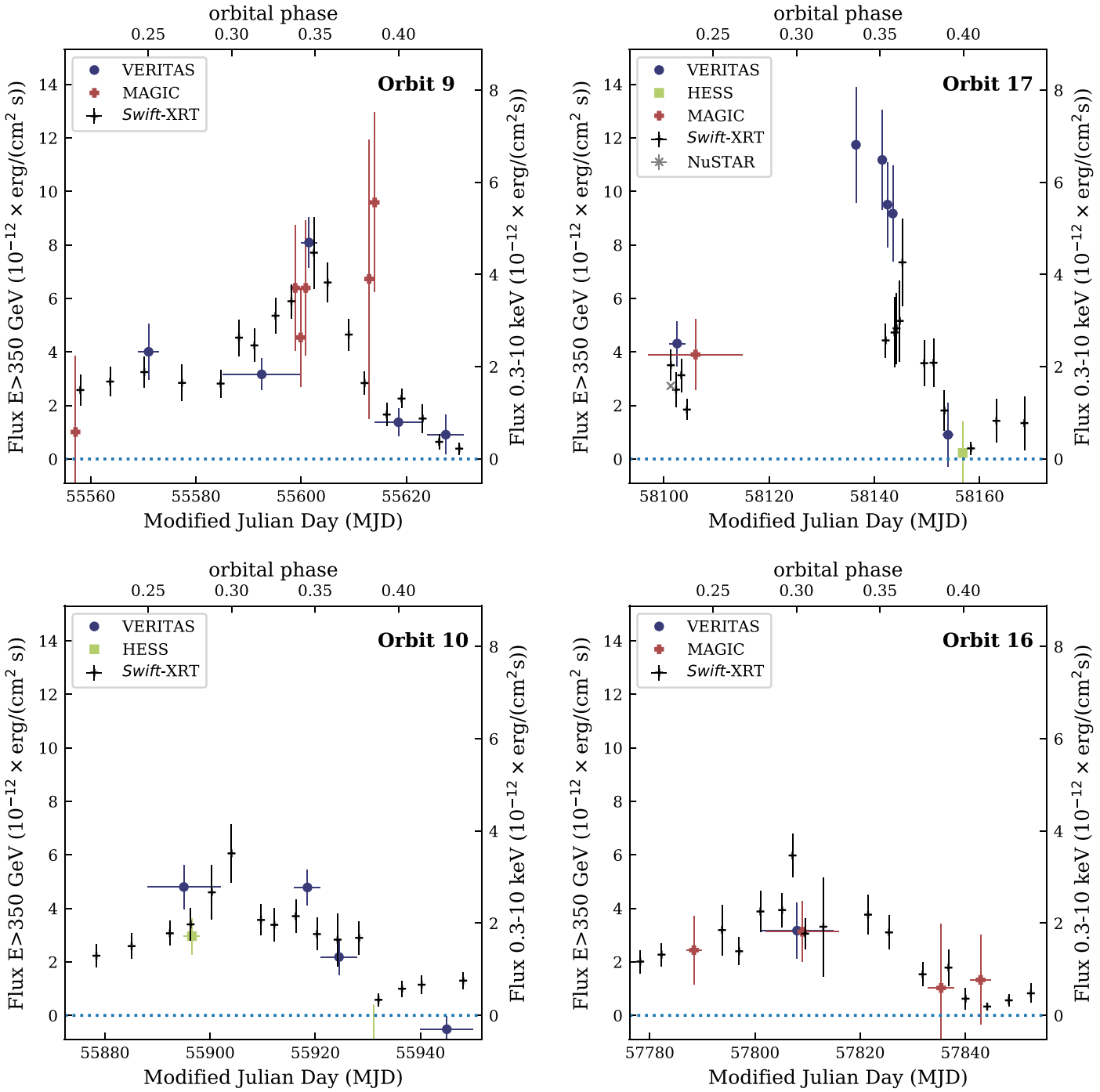

Figure 9. Detailed light curves for four orbits with deep X-ray and gamma-ray coverage in gamma-rays (H.E.S.S., MAGIC, VERITAS, >350 GeV; left axis) and X-rays (NuSTAR, Swift-XRT, 0.3–10 keV; right axis). Orbits are numbered following the start of the gamma-ray observations (phase zero of orbit 1 is at MJD 52,953). The orbits 9 and 17 (upper two panels) represent high states of the source while the orbits 10 and 16 (lower two panels) represent low states. Vertical lines indicate statistical uncertainties. Fluxes are averaged over time intervals indicated by the horizontal lines (for most flux points smaller than the marker size). An orbital period of 317.3 days is assumed.

least disturbed by the winds of the massive star. For the orbital solution proposed by Moritani et al. (2018), instead, the first maximum is after apastron and the second maximum shortly after periastron. A direct comparison with other gamma-ray binaries is affected by these uncertainties. However, it is worth pointing out that the two other long-period systems known (PSR B1259-63/LS 2883 and PSR J2032 + 4127/MT91 213) show their emission maxima close to or around the periastron passages.

The analysis of a total of 59 X-ray–VHE flux pairs reveals a strong correlation between these two energy bands (Figure 5, top). No time lag is observed (Figure 5, bottom), although the grouping of the gamma-ray observations (to gain statistics) prevents us from probing time lags $\tau \leqslant 10$ days. The X-ray–VHE correlation suggests that emission in both bands is produced by the same population of accelerated particles. One-zone leptonic models can describe the X-ray to TeV spectral distribution and the correlation between these two energy bands

Table 5
Summary of Observations and Spectral Analyses at Gamma-Ray Energies for Orbits 9 and 17

MJD Range	Exposure (hr)	Significance[a] (σ) (pre-trial)	Flux Normalization Constant at 0.5 TeV [cm^{-2} s^{-1} TeV^{-1}]	Photon Index	χ^2/N
VERITAS observations of orbit 9 (2011 Jan)					
55,585–55,600	11.3	6.1	$(3.8 \pm 0.9) \times 10^{-12}$	2.71 ± 0.30	2.7/3
55,600–55,603	8.7	11.6	$(8.3 \pm 1.2) \times 10^{-12}$	2.69 ± 0.17	4.5/4
MAGIC observations of orbit 9 (2011 Jan)					
55,585–55,600	4.5	5.9	$(4.9 \pm 0.9) \times 10^{-12}$	2.48 ± 0.20	4.2/3
VERITAS observations of orbit 17 (2018 Jan)					
58,136	1.8	7.5	$(11.9 \pm 2.6) \times 10^{-12}$	2.22 ± 0.24	3.3/4
58,141	2.5	7.7	$(9.2 \pm 2.2) \times 10^{-12}$	2.20 ± 0.24	2.0/4
58,142	3.6	7.8	$(11.6 \pm 2.4) \times 10^{-12}$	2.56 ± 0.28	1.5/3
58,143	3.1	5.8	$(7.3 \pm 2.0) \times 10^{-12}$	2.15 ± 0.22	3.2/2

Note. The table lists the results of the power-law fits to the differential energy spectra obtained for VERITAS and MAGIC. Errors are 1σ statistical errors only. The systematic errors are 11%–20% on the flux constant and 0.10–0.15 on the spectral index.
[a] Significances are calculated following the maximum likelihood ratio test method proposed in Li & Ma (1983).

in HESS J0632 + 057, as seen in Hinton et al. (2009), Aleksić et al. (2012), and Aliu et al. (2014). In this scenario, a population of electrons produces X-rays via synchrotron emission and VHE gamma-rays through inverse Compton scattering off thermal photons from the companion Be star. It has been shown in Archer et al. (2020) that a one-zone leptonic model can describe well a small set of contemporaneous SED data in hard X-rays and VHE gamma-rays observed with NuSTAR and with VERITAS, respectively.

One of the main difficulties in modeling HESS J0632 +057's SED data lies in accounting for the observed orbit-to-orbit variability. Detailed hydrodynamical simulations of HESS J0632 + 057 by Bosch-Ramon et al. (2017) and Barkov & Bosch-Ramon (2018) propose a trapping of parts of the shocked pulsar wind by the massive star as a cause of orbit-to-orbit variability. These authors suggest that the peaks of the X-ray and VHE gamma-ray emission are a consequence of the accumulation of the hot shocked plasma injected by the shocked pulsar wind and the consequent disruption of the spiral arm in the periastron–apastron direction. It is proposed that the observed drop in the X-ray and gamma-ray fluxes is caused by the disruption of the stellar wind by the pulsar wind. In the simpler model of of Archer et al. (2020), this variability is assumed to be due to fluctuations of the electron density in the emission zone, which is treated as a free parameter of the fit. This kind of approach can only be applied to contemporaneous X-ray and VHE gamma-ray observations and it is only possible because of the large overlap between the electron energies responsible for the X-rays and VHE gamma-rays in this leptonic scenario.

For the first time, contemporaneous X-ray and gamma-ray observations have been presented for orbital phases 0.2–0.45 (around first maximum and minimum) for four different orbits (Figures 9 and 10). The measurements suggest that flux levels are different between these periods, indicating the existence of orbit-to-orbit variability in the emission pattern. No evidence for a superorbital period, as observed, e.g., in the gamma-ray binary LS I +61° 303 (Ahnen et al. 2016), is found. On shorter integration times, strong variability of the VHE flux on timescales of a few days was seen during observations in 2011 (orbit 9) and 2018 (orbit 17) at orbital phase ∼0.35 (prior to the local flux minimum; see Figure 9). Similar day-scale variability has been detected during VERITAS observations of the apastron passage of the compact object in the LS I +61° 303 binary system (Archambault et al. 2016).

In the GeV band, the weak flux of HESS J0632 + 057 hinders the detection of orbital variability with the Fermi-LAT (Li et al. 2017). No variability pattern is seen in Hα equivalent width, whereas the radial velocity and the Hα FWHM increase in the orbital phase range 0.3–0.6 and decrease between 0.7 and 0.3. The data demonstrate (with low statistical significance) a somewhat higher scatter at $\phi > 0.5$, which may indicate a perturbed state of the stellar disk at these orbital phases. The correlation coefficients obtained for the different Hα parameters (EW, FWHM, and centroid velocity) and X-ray or VHE emission do not show significant values for the observed time lags (Figure 6). Optical spectroscopic measurements of MWC 148 during and after the time of the high state around 2018 January 25 with the RCC telescope at Rozhen NAO, Bulgaria, indicate changes in the structure or size of the equatorial disk of the Be star (Stoyanov et al. 2018), although comparable measurements have been carried out only during different orbital phases (2018 January 25: phase 0.36 and 2014 January 23: phase 0.71). Measurements of equivalent width by the Southern African Large Telescope (SALT Transient Program, L. Townsend 2020 personal communication) confirm this: pointings with a measured |EW| of >40 Å in 2018 February indicate a larger circumstellar disk than at the same phase in earlier cycles (e.g., |EW| of 2017 March 28 was ≈30 Å; see also measurements by Casares et al. 2012; Moritani et al. 2015).

4.3. Comparison with Other Binaries and Model Descriptions

Similarities of the emission pattern observed for HESS J0632 + 057 with those of other gamma-ray binaries are notable. Similar correlations between X-rays and VHE emission have been found during an outburst of LS I +61° 303 (Anderhub et al. 2009), but not consistently across different orbits (Acciari et al. 2011). However, many

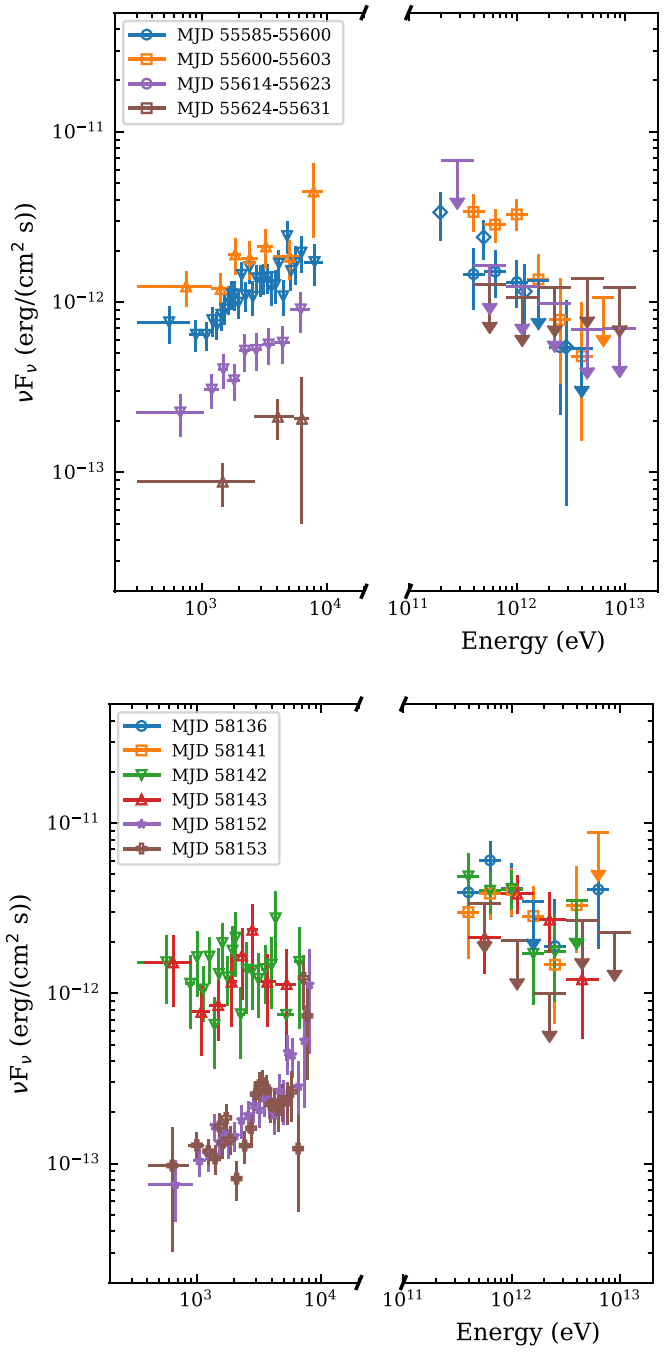

Figure 10. Spectral energy distribution for HESS J0632 + 057 during two orbital period ranges (orbit 9: top panel; orbit 17: bottom panel) with deep coverage in X-ray (Swift-XRT) and gamma-ray observations. Gamma-ray spectra obtained by VERITAS are shown in all figures. Orbit 9 also shows results from MAGIC (Aleksić et al. 2012), indicated by diamond-shaped markers. Downward pointing arrows indicate upper limits at the 95% confidence level.

short-period systems like LS I +61° 303 are characterized by single-maximum light curves (Dubus 2013), while long-period gamma-ray binaries (e.g., PSR B1259-63/LS 2883, PSR J2032 + 4127/MT91 213) show a similar double-peaked structure in X- and gamma-ray emission (see, e.g., Dubus 2013; Abeysekara et al. 2018; H.E.S.S. Collaboration et al. 2020) as observed in HESS J0632 + 057. Moritani et al. (2018) and Malyshev et al. (2019) compare the emission patterns of HESS J0632 + 057 with those of PSR B1259-63/LS 2883 and relate the double-peak structure of the orbital-phase-folded light curves in the keV–VHE bands in both systems to the inclined disk geometry and the change in environmental parameters during the first and second crossings of the circumstellar disk by the compact object. The higher ambient density and increased magnetic field strengths in the stellar equatorial wind zone lead to enhanced particle acceleration via wind–wind interaction and possibly increased radiation efficiency due to an increased energy loss timescale for the electron population. Close to periastron, when the compact object leaves the disk, acceleration and radiation efficiency decrease, leading to the dip in the keV and VHE light curves. An & Romani (2017) obtain a quantitative description of the orbital variability pattern in X-rays of the binary 1FGL J1018.6-5856, which shows a similar double-peaked structure to that observed in HESS J0632 + 057. The model used a simple leptonic model based on intrabinary shock emission as discussed in the previous section, but with the following modifications: two electron populations are assumed, where one moves slowly in the shock and the other is accelerated along the shock flow; beaming effects, as proposed by Dubus et al. (2010), are added to the accelerated component in the cone-shaped shock front. Applying this model to HESS J0632 + 057, these components would lead to the enhanced flux state around orbital phases of 0.7–0.9 (when the flow direction and the line of sight align). The stellar disk of the Be star in HESS J0632 + 057 is the main difference compared to the diskless O-star in 1FGL J1018.6-5856 and might lead to enhanced absorption of the X-ray and gamma-ray emission. Additional changes in the magnetic fields at the intrabinary shock position due to the eccentric orbit and the resulting change in acceleration efficiency might be important to provide favourable conditions for the high emission state around phases 0.3–0.4 (Tokayer et al. 2021).

An alternative scenario to explain the variability pattern of HESS J0632 + 057 could be provided by flip-flop models. Torres et al. (2012) and Papitto et al. (2012) proposed this scenario to explain the emission from LS I +61° 303. In this scenario, the compact object is a pulsar. Different authors support the pulsar nature of the compact object in HESS J0632 + 057 (see Mochol & Kirk 2014; Moritani et al. 2015), as might be the case for the binaries LS I +61° 303 and LS 5039 (Yoneda et al. 2020), or as in the confirmed pulsar binaries PSR B1259-63/LS 2883 (Johnston et al. 1992; Kirk et al. 1999) and PSR J2032 + 4127/MT91 213 (Abdo et al. 2009; Camilo et al. 2009). In the model proposed by Torres et al. (2012) for LS I +61° 303, the pulsar switches from a propeller regime at periastron to an ejector regime at apastron, which is triggered by changes in the mass-loss rate of the companion star. Hence, for periods when the disk is at its largest, the propeller regime could be active also at apastron, reducing or impeding VHE emission and explaining the long-term variability in the binary. It should be noted that a recent Astronomer's Telegram (Weng et al. 2021) reported on the detection of a periodicity from LS I +61° 303 at a period 269.196 ms. This period is almost exactly that marked as the preferred one for the flip-flop model to work (see Figure 4 of Papitto et al. 2012). In this model, optical and VHE emissions are predicted to be anticorrelated. Moritani et al. (2015) argued that a similar mechanism could work in HESS J0632 + 057, although the orbital phases in which the gamma-ray emission occurs are different due to the geometry of the system. In the case of HESS J0632 + 057, the strong gas pressure will

overcome the pulsar-wind pressure at periastron, suppressing VHE emission (assuming the ephemerides of Casares et al. 2012). The second minimum will take place at apastron, where the photon field and magnetic field density are low. In the case of LS I +61° 303, Ahnen et al. (2016) found the VHE periodicity as predicted, but no hints for (anti)correlation between optical and VHE were observed. The latter could be the result of the strong, short-timescale intraday variation displayed by the Hα fluxes. In HESS J0632 + 057, a similar situation can be at work, since both the contemporaneity of the observations (5 day time span) and the integration times are large, even more than for the case of LS I +61° 303, and were already problematic. The lack of (anti)correlation between optical and high-energy emission (X- and gamma-rays) observed in HESS J0632 + 057 can also be explained by the difference in the integration times required at these frequencies, which is in agreement with the results found by Ahnen et al. (2016) for the case of LS I +61° 303.

Regardless of the assumed model and the nature of the compact object, two additional processes can affect the orbital modulation of VHE emission, namely gamma–gamma absorption processes and the anisotropic nature of inverse Compton radiation. Close to periastron, the increased soft photon density can produce severe gamma–gamma absorption losses, which are potentially able to explain dips in the light curves of several gamma-ray binary systems (see, e.g., Böttcher & Dermer 2005; Dermer & Böttcher 2006; Sushch & van Soelen 2017). Anisotropic inverse Compton effects are important for orientations close to edge-on, as suggested by Bednarek (2006). In the context of LS 5039, Khangulyan et al. (2008) and Dubus et al. (2008) have shown that a model taking into account both effects can reproduce well the observed orbital light curve, producing somewhat different results to the spectrum in the isotropic inverse Compton case at inferior and superior conjunctions. The observed cutoff in the energy spectrum for the orbital phase bin 0.2–0.4 at $E_c = 1.75 \pm 0.38$ TeV can have multiple, possibly correlated, origins: limiting properties of the shock determining the acceleration efficiency and the maximum energy of accelerated particles; photon fields determining the absorption of multi-TeV gamma-rays; or the effective temperature distribution of the low-energy target photons (e.g., due to substantial contribution from the stellar disk), which impact the energy of the gamma-rays obtained from inverse Compton processes.

An additional channel of information that can allow the proposed models to be discriminated against each other is the observation of flux variability patterns and outbursts at shorter timescales than the orbital period, as shown in Figure 9. Such variability suggests a rapid change in the environmental properties leading to particle acceleration, or in the surrounding medium impacting the VHE emission, possibly because of a peculiar geometry in the system (e.g., beaming, as proposed for PSR B1259-63/LS 2883 in, e.g., Khangulyan et al. 2011; Chernyakova et al. 2020). In terms of the discussed models, however, short-term variability can be accommodated by several theoretical explanations. In the flip-flop scenario these timescales could be interpreted as the timescales on which the pulsar wind is quenched due to increased circumstellar disk density. In the PSR B1259-63/LS 2883-like model, the same timescales would correspond to the times at which the compact object intersects the disk's region of influence and exits from it close to periastron. Additionally, stellar winds of massive stars can exhibit strong density variations. Flux variability can be connected to the clumpiness of the equatorial or isotropic stellar wind, which can lead to keV–VHE flux changes; see, e.g., Paredes-Fortuny et al. (2015a) and Archambault et al. (2016). In this case the variability time can allow us to estimate the characteristic size of the corresponding high-density structure. Deeper, simultaneous multiwavelength (keV–GeV–VHE) observations of HESS J0632 + 057 with current or future facilities can help to clarify these points. Such observations may allow one to find the shortest timescales of variability in each band and more firmly establish the similarities and differences in the variability patterns. Additional future Hα observations used as a tracer for the radius of the circumstellar disk are also helpful, since the data set shown in this paper is rather sparse.

5. Summary and Conclusions

The results of the deepest study of the gamma-ray binary HESS J0632 + 057 at TeV energies with H.E.S.S., MAGIC, and VERITAS, comprising a total of 450 hr of data spanning almost 15 yr, are presented. This multiyear campaign is embedded in a multiwavelength context, which includes X-ray (Swift-XRT, Chandra, XMM-Newton, NuStar, and Suzaku) and optical Hα observations. The results of the spectral and temporal analyses are summarized as follows.

1. For the first time, the orbital period at TeV energies was determined, yielding a value of 316.7 ± 4.4 days. This solution is in agreement with the 317.3 ± 0.7 day period derived from the latest Swift-XRT X-ray data set.
2. The light curve and spectral energy distribution along the orbit were characterized. In the phase-folded light curve, two well-differentiated peaks are visible, together with a dip phase and a broader plateau phase. The VHE SEDs for all of these phases (except the dip phase, where only upper limits could be derived) are generally characterized as power laws, showing no variability in the spectral slope within statistical errors. Only the spectrum measured with VERITAS during the phases 0.2–0.4 favors a power law with exponential cutoff at 1.75 TeV.
3. The strong correlation between X-rays and gamma-rays suggests a common origin of the radiation, indicating the existence of a single population of particles. An indication for an X-ray source partially unrelated to the gamma-ray emission was found, however.
4. The lack of correlation between Hα and X-rays or gamma-rays might point toward a negligible role for the disk of the Be star in the modulation of the nonthermal emission, but is possibly an effect of the fast variability of Hα compared with the sparse overlap of the data sets at different energies. If the Hα spectra change on a timescale of days, much shorter than the grouped gamma-ray timescales, one cannot measure a possible correlation with the sensitivity of current VHE/TeV instruments.
5. The ratio of gamma-ray to X-ray flux underlines the equality or even dominance of the gamma-ray energy range for the emission of HESS J0632 + 057.
6. Two outbursts during orbits 9 (2011 January) and 17 (2018 January) revealed enhanced gamma-ray and X-ray emission comparable to the highest flux ever observed from this binary. Furthermore, a flux decay time of

roughly 20 days or less was detected for two orbits. Contemporaneous Hα data taken on 2018 January 25 indicate that the size of the circumstellar disk had increased during those days, suggesting that the decretion disk was larger and its structure had changed.

Looking forward, it is obvious that deeper, simultaneous multiwavelength (Hα and keV–GeV–TeV) observations of HESS J0632 + 057 with current and/or future more-sensitive instruments are required to characterize its emission. The determination of the orbital geometry of the system is of utmost importance and requires a coordinated multiyear optical campaign. Finally, the wealth of data presented for HESS J0632 + 057 awaits theoretical modeling taking consistently all aspects of the spectral and temporal measurements into account.

The support of the Namibian authorities and of the University of Namibia in facilitating the construction and operation of H.E.S.S. is gratefully acknowledged, as is the support by the German Ministry for Education and Research (BMBF), the Max Planck Society, the German Research Foundation (DFG), the Helmholtz Association, the Alexander von Humboldt Foundation, the French Ministry of Higher Education, Research and Innovation, the Centre National de la Recherche Scientifique (CNRS/IN2P3 and CNRS/INSU), the Commissariat à l'énergie atomique et aux énergies alternatives (CEA), the U.K. Science and Technology Facilities Council (STFC), the Knut and Alice Wallenberg Foundation, the National Science Centre, Poland grant no. 2016/22/M/ST9/00382, the South African Department of Science and Technology and National Research Foundation, the University of Namibia, the National Commission on Research, Science & Technology of Namibia (NCRST), the Austrian Federal Ministry of Education, Science and Research and the Austrian Science Fund (FWF), the Australian Research Council (ARC), the Japan Society for the Promotion of Science, and the University of Amsterdam. We appreciate the excellent work of the technical support staff in Berlin, Zeuthen, Heidelberg, Palaiseau, Paris, Saclay, Tübingen, and Namibia in the construction and operation of the equipment. This work benefited from services provided by the H.E.S.S. Virtual Organisation, supported by the national resource providers of the EGI Federation.

The MAGIC collaboration would like to thank the Instituto de Astrofísica de Canarias for the excellent working conditions at the Observatorio del Roque de los Muchachos in La Palma. The financial support of the German BMBF, MPG and HGF; the Italian INFN and INAF; the Swiss National Fund SNF; the ERDF under the Spanish Ministerio de Ciencia e Innovación (MICINN) (PID2019-104114RB-C31, PID2019-104114RB-C32, PID2019-104114RB-C33, PID2019-105510GB-C31, PID2019-107847RB-C41, PID2019-107847RB-C42, PID2019-107988GB-C22); the Indian Department of Atomic Energy; the Japanese ICRR, the University of Tokyo, JSPS, and MEXT; the Bulgarian Ministry of Education and Science, National RI Roadmap Project DO1-268/16.12.2019 and the Academy of Finland grant nr. 320045 is gratefully acknowledged. This work was also supported by the Spanish Centro de Excelencia "Severo Ochoa" (SEV-2016-0588, CEX2019-000920-S), the Unidad de Excelencia "María de Maeztu" (CEX2019-000918-M, MDM-2015-0509-18-2), and the CERCA program of the Generalitat de Catalunya; by the Croatian Science Foundation (HrZZ) Project IP-2016-06-9782 and the University of Rijeka Project 13.12.1.3.02; by the DFG Collaborative Research Centers SFB823/C4 and SFB876/C3; the Polish National Research Centre grant UMO-2016/22/M/ST9/00382; and by the Brazilian MCTIC, CNPq and FAPERJ.

VERITAS is supported by grants from the U.S. Department of Energy Office of Science, the U.S. National Science Foundation and the Smithsonian Institution, by NSERC in Canada, and by the Helmholtz Association in Germany. We acknowledge the excellent work of the technical support staff at the Fred Lawrence Whipple Observatory and at the collaborating institutions in the construction and operation of the instrument. This research used resources provided by the Open Science Grid, which is supported by the National Science Foundation and the U.S. Department of Energy's Office of Science, and resources of the National Energy Research Scientific Computing Center (NERSC), a U.S. Department of Energy Office of Science User Facility operated under Contract No. DE-AC02-05CH11231.

D.F.T. acknowledges support by grants PGC2018-095512-B-I00, SGR2017-1383, and AYA2017-92402-EXP.

This research has made use of data obtained from the Chandra Data Archive and the Chandra Source Catalog; it has made use of data obtained from the Suzaku satellite, a collaborative mission between the space agencies of Japan (JAXA) and the USA (NASA); it is based on observations obtained with XMM-Newton, an ESA science mission with instruments and contributions directly funded by ESA Member States and NASA; it made use of data from the NuSTAR mission, a project led by the California Institute of Technology, managed by the Jet Propulsion Laboratory, and funded by the NASA.

Facilities: Swift, XMM-Newton, CXO, Suzaku, NuSTAR, MAGIC, H.E.S.S., VERITAS, CFHT, OAO:1.88m .

Software: Astropy (version 3.01, Astropy Collaboration et al. 2013, 2018), CIAO (v.4.9, Fruscione et al. 2006) Eventdisplay (v4.83, Maier & Holder 2017), HEAsoft (v6.22, HEASARC 2014), IRAF (Tody 1986), PyAstronomy (version 0.13, Czesla et al. 2019), xrtpipeline (v.0.13.4), XSPEC (v12.9.1 m, Arnaud 1996).

Availability of Data

The data sets generated and analyzed during the current study are available through the websites of the HESS J0632 + 057[121], MAGIC[122], and VERITAS[123] Instruments and from the Zenodo data repository at https://doi.org/10.5281/zenodo.5157848.

Appendix A
Determination of Orbital Period

Literature provides a variety of methods for periodicity analysis of sparse astronomical data (e.g., Graham et al. 2013). The performance of the different techniques depends on quality, coverage, and shape of the given light curves. There is no clear guidance which technique is best for a given data set. For these reasons, the following methods are evaluated using Monte Carlo-generated light curves: discrete correlation

[121] https://www.mpi-hd.mpg.de/hfm/HESS/pages/publications/auxiliary/auxinfo_hessj0632_HMVdata.html
[122] http://vobs.magic.pic.es/fits/
[123] https://github.com/VERITAS-Observatory/VERITAS-VTSCat

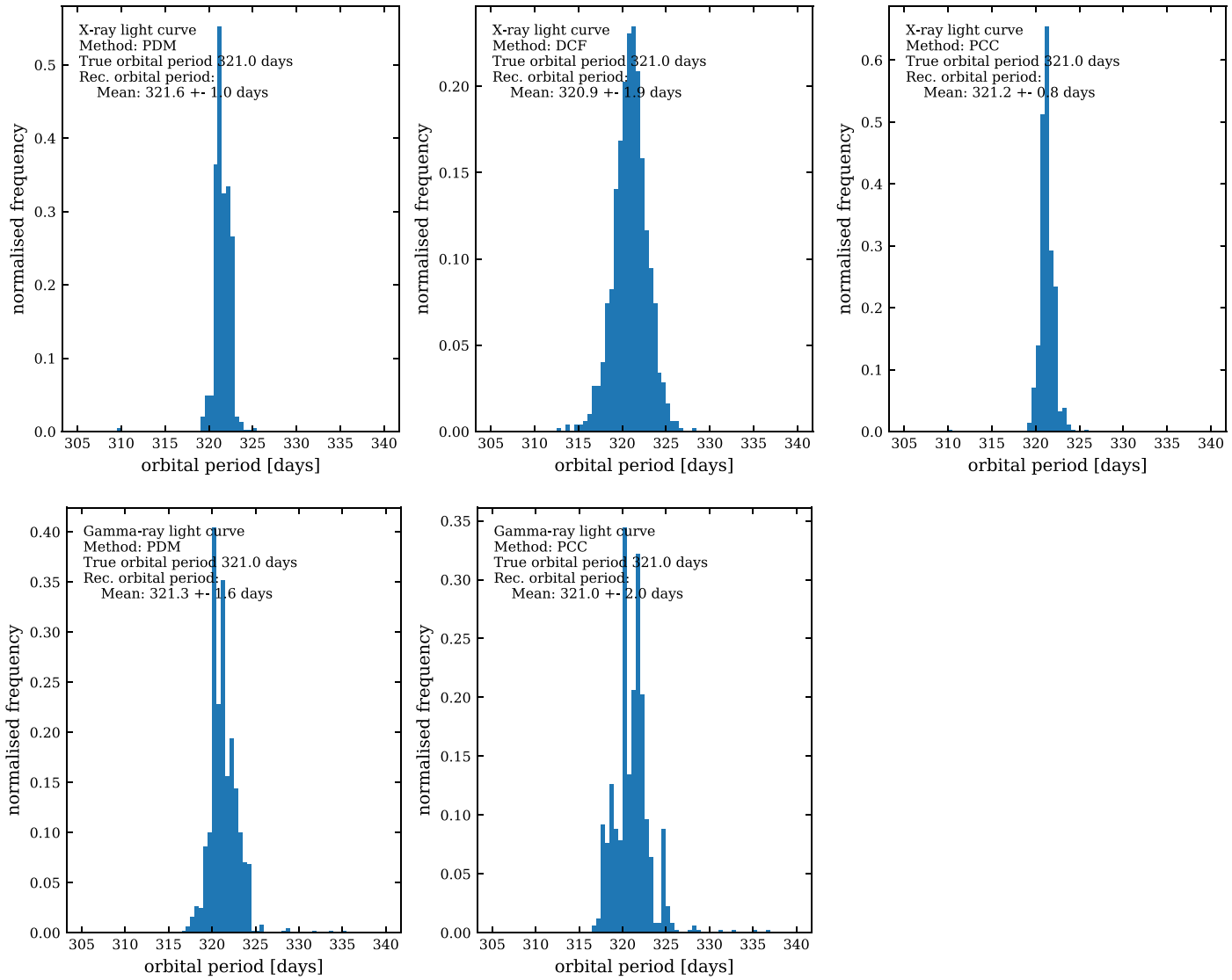

Figure 11. Outcome of the analysis of 1000 Monte Carlo-generated light curves using the following data sets as templates for the toy MC. Top: Swift-XRT; bottom: VERITAS and H.E.S.S. In all cases a true orbital period of 321 days is assumed. Different techniques for periodicity analysis, as indicated in the figure panels, have been applied to the same MC-generated light curves. Results are given as both mean and 68% fiducial interval for all methods.

functions (DCF, Edelson & Krolik 1988; Robertson et al. 2015),[124] correlation analysis comparing the light curves with a binned-average light curve (PCC, Malyshev et al. 2019), Lomb–Scargle periodograms (Lomb 1976; Scargle 1982),[125] and the phase dispersion minimization method (PDM, Stellingwerf 1978).[126]

The Monte Carlo-generated light curves are based on the phase-binned average profiles of the observed fluxes in X- or gamma-rays and are generated assuming the same distribution in time as the measurements, with flux values randomly altered according to the corresponding uncertainties. As the phase-binned averaged profile removes variability that is not due to statistical uncertainties of the measurement, additional power-law noise following a $(1/f)^{1.2}$ spectrum is added (Timmer & Koenig 1995).

Figure 11 shows the results of the different techniques applied to 1000 Monte Carlo-generated light curves based on the Swift-XRT and gamma-ray data sets assuming a true orbital period of 321 days. The search region is restricted to a $\pm$30 day interval around the true orbital period. This prior is necessary, because the PDM method tends toward reconstructing from a significant fraction (>20%) of light curves an orbital period that is roughly half the true orbital period. Applying the method of Lomb and Scargle to the generated light curves leads to inconsistent results, because the largest peak in the periodograms for most light curves is at half the true period. This result is also obtained when applying this method to the Swift-XRT data. Folding the light curve with such short periods leads to inconsistent solutions, because both the PDM and Lomb–Scargle methods ignore its nonsinusoidal shape and in particular the very low fluxes or nondetections of the system visible at orbital phases of $\approx$0.4 (assuming an orbital period of 317.3 days).

[124] The implementation of the DCF method in the Python package pyDCF (https://github.com/astronomerdamo/pydcf) is used.
[125] The implementation of the Lomb–Scargle method in astropy is used (https://docs.astropy.org/en/stable/timeseries/lombscargle.html).
[126] The implementation of the PDM method in the Python package PyAstronomy (https://github.com/sczesla/PyAstronomy) is used.

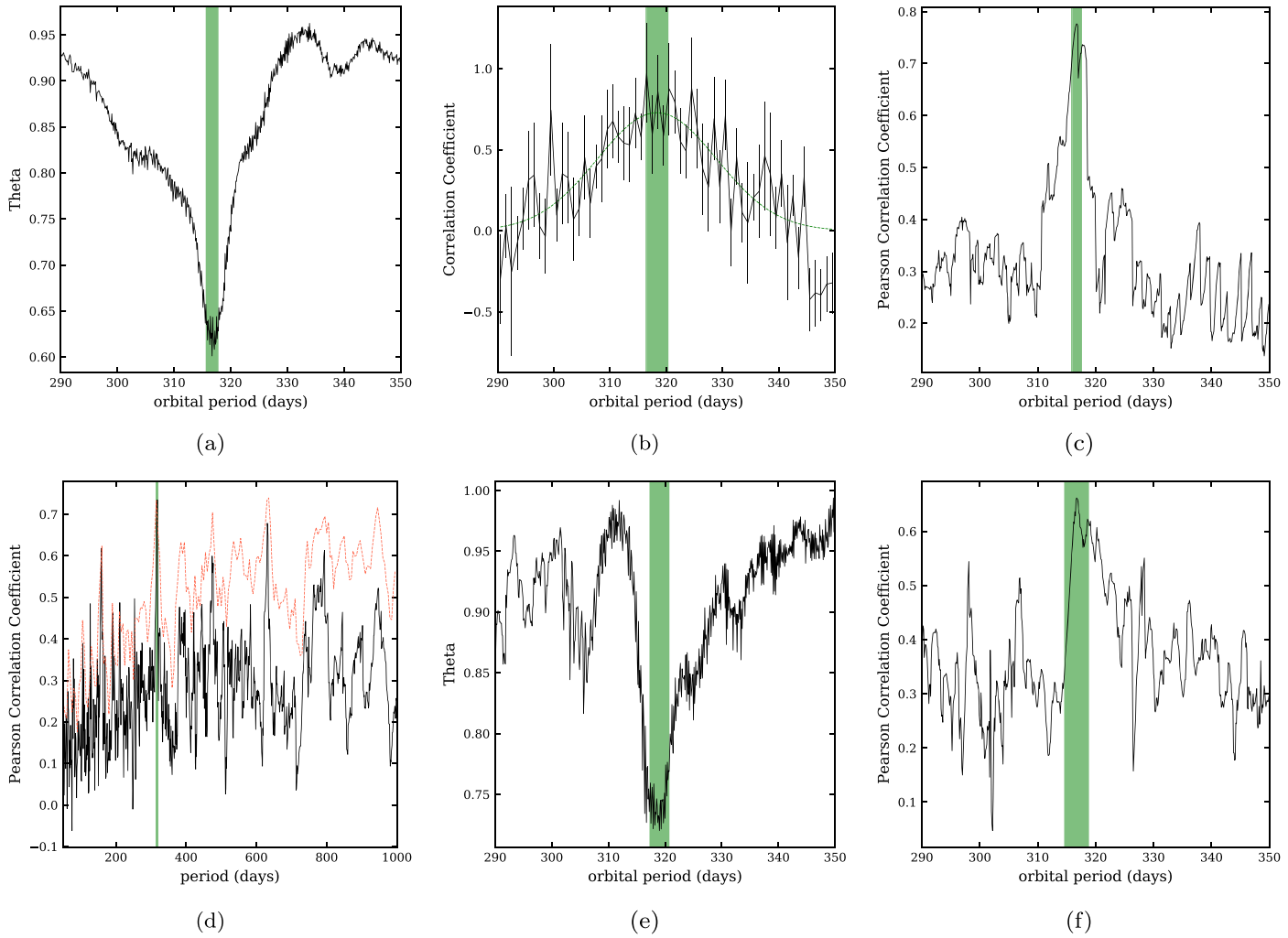

Figure 12. Results of the periodicity analysis of (a)–(d) Swift-XRT and (e)–(f) gamma-ray measurements, applying different methods: (a) Phase dispersion (PDM; Swift-XRT); (b) discrete correlation coefficient (DCF; Swift-XRT); (c) Pearson correlation coefficient (PCC; Swift-XRT); (d) search for periods other than the orbital period in the range 50 to 1000 days; Pearson correlation coefficient (PCC; Swift-XRT); the red dashed line indicates the 99% containment level obtained from Monte Carlo sets of the XRT light curve (to take spectral leakage into account, an orbital periodicity of 317.3 days is assumed in the Monte Carlo sets); (e) phase dispersion (PDM; gamma-ray energies); (f) Pearson correlation coefficient (PCC; gamma-ray energies). All coefficients are plotted as a function of orbital period. The green shaded areas indicate the 68% fiducial interval obtained by the analysis of MC-generated light curves (see text for details).

All shown methods are able to reconstruct, for the majority of the MC light curves, the true orbital period with an uncertainty of less than 2 days for the Swift-XRT and gamma-ray data set. The DCF method does not provide reliable estimations when applied to the gamma-ray measurements or to the toy MC based on the gamma-ray data. This is probably due to the sparsity of the gamma-ray data set and the larger uncertainties of the flux measurements. Statistical uncertainties for the given data sets are derived from the 68% fiducial intervals of the corresponding toy MC analysis. Systematic uncertainties are derived from the largest difference to the expected values (0.6 days) and the impact of the choice of the bin width on the calculation of the averaged light curves. Bin widths from 0.025 to 0.1 in orbital phase are tested and the largest difference is used to estimate the contribution to the systematic uncertainties. The total systematic uncertainty for the determination of orbital period is estimated to be $\delta_{\rm sys}^{\rm Swift\ XRT} = 1.5$ days and $\delta_{\rm sys}^{\rm Gamma} = 2.5$ days.

Confidence limits on the correlation coefficients are obtained in a similar fashion: 1000 toy MC light curves with similar data structure to the one obtained by observations are used to calculate the 95% and 99% quantiles. Two null hypotheses are distinguished: a constant flux is assumed for the determination of the statistical significance of the correlation coefficients for the analysis of the orbital period (see Figure 12(c)). For the search for modulation periods other than the orbital period, toy MC light curves as described above, including the average observed orbital modulation pattern, are generated and analyzed with the different methods of determining the different periods (see Figure 12(d)).

Figure 12 shows the results of application of all three techniques on the Swift-XRT and gamma-ray light-curve measurements (see Figure 2). A summary of all obtained orbital periods together with those reported in the literature is given in Table 3.

Appendix B
Impact of Orbital Period Uncertainty on Phase-folded Light Curves

Uncertainties on the determination of the orbital period might lead to significant differences in the shape of the phase-folded light curves given the long total observation time of ≈15 yr for gamma-ray and ≈10 yr for X-ray measurements. To test this, four different orbital periods are assumed: $P_+ = 319.5$ days, $P_- = 315.1$ days, $P_M = 313$ days, and $P_{H\alpha} = 308$ days. P_+ and P_- correspond to a change in the orbital period by 1σ statistical error plus the systematic uncertainty; P_M and $P_{H\alpha}$ correspond to the solutions presented in Moritani et al. (2018).

Figures 13 and 14 show the impact of the variation of the assumed orbital period: the three most prominent features of a peak around phases 0.3, a minimum around phase 0.4, and a second maximum region around phase 0.6 are clearly visible in all cases. This shows that the choice of $P_{orb} = 317.3$ days does not influence the discussion of the physical properties presented in this work, except for the shortest period of 308 days. It should be noted that assuming such a short orbital period, as derived from optical Hα observations (Moritani et al. 2018),

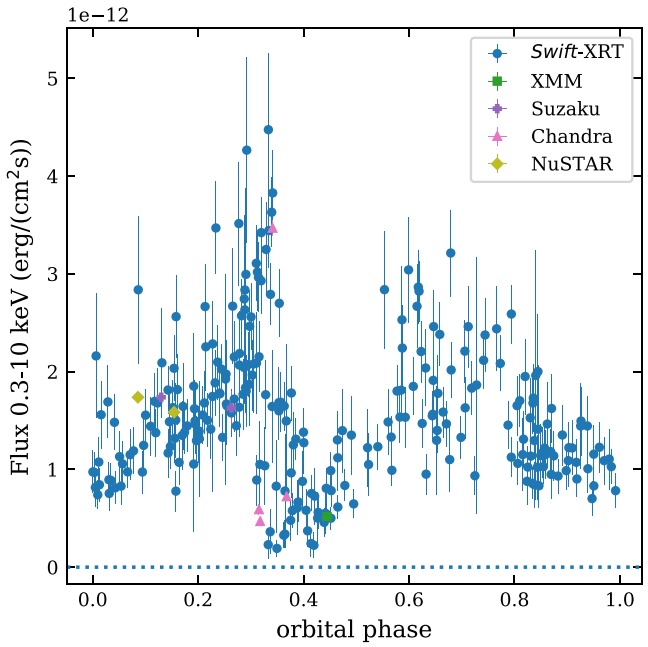

(a) X-rays ($P = 319.5$ days)

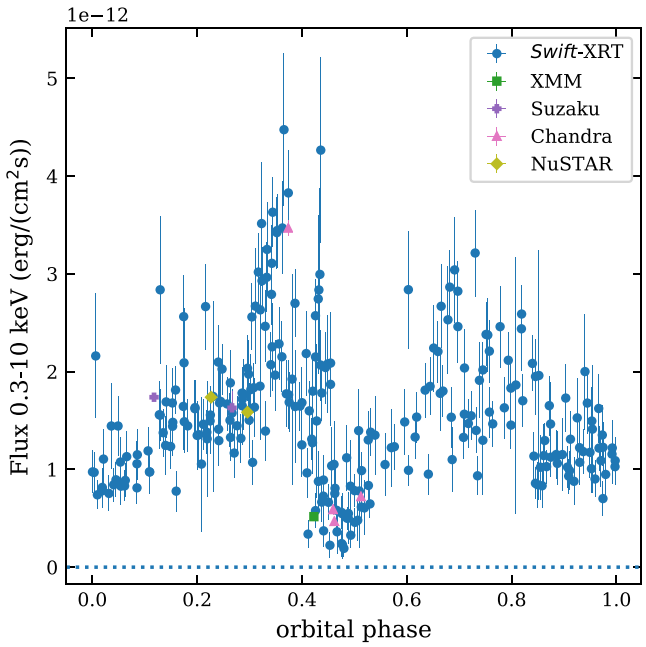

(b) X-rays ($P = 315.1$ days)

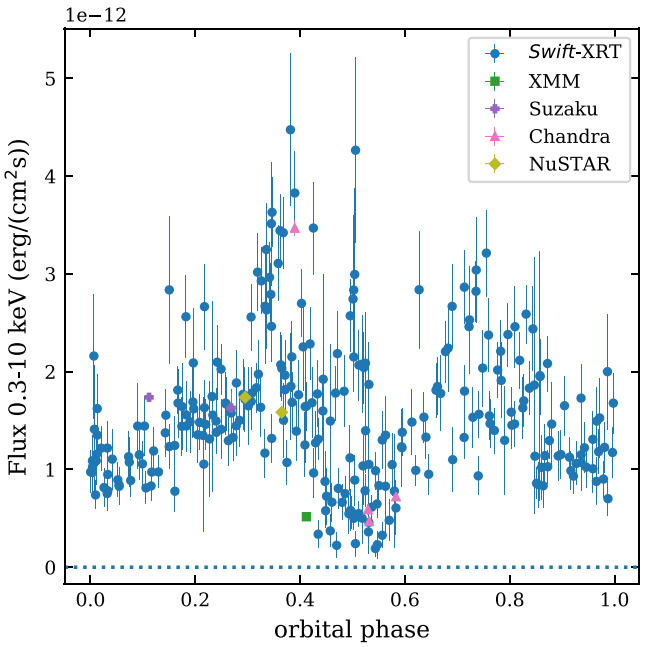

(c) X-rays ($P = 313$ days)

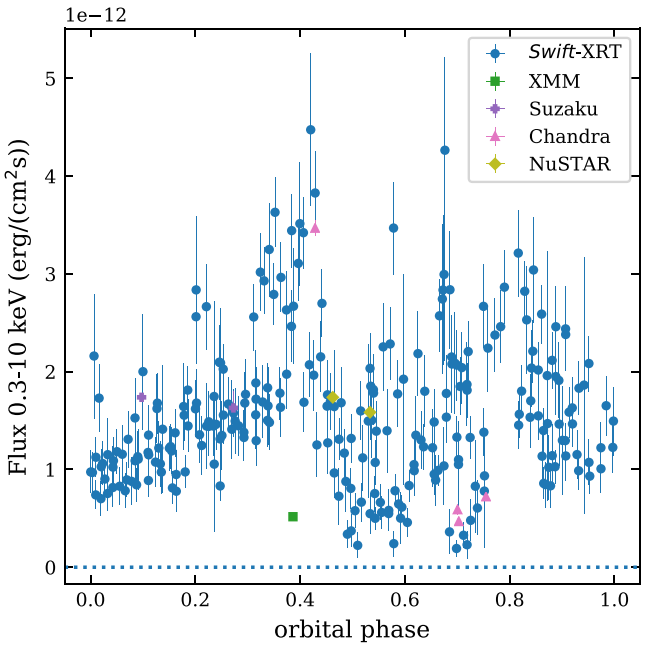

(d) X-rays ($P = 308$ days)

Figure 13. X-ray (0.3–10 keV) light curves as function of orbital phase assuming orbital periods as indicated below the plots. For further details, see Figure 3 and text.

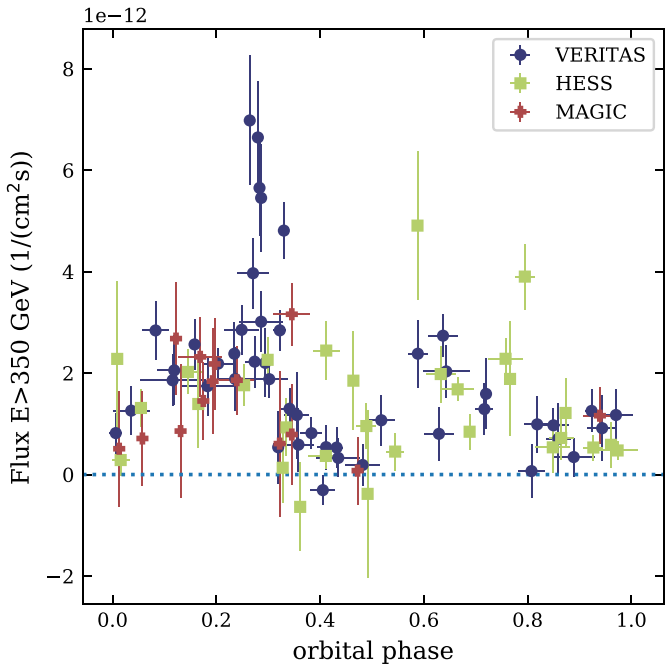

(a) Gamma-rays ($P = 319.5$ days)

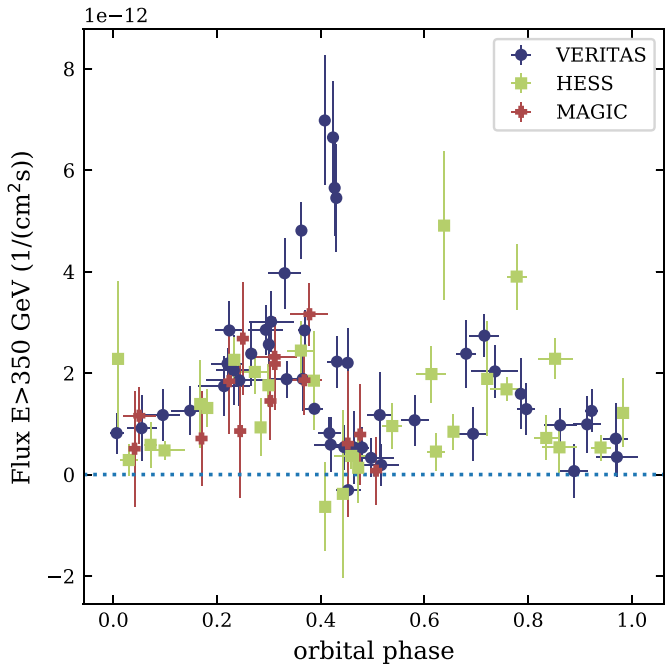

(b) Gamma-rays ($P = 315.1$ days)

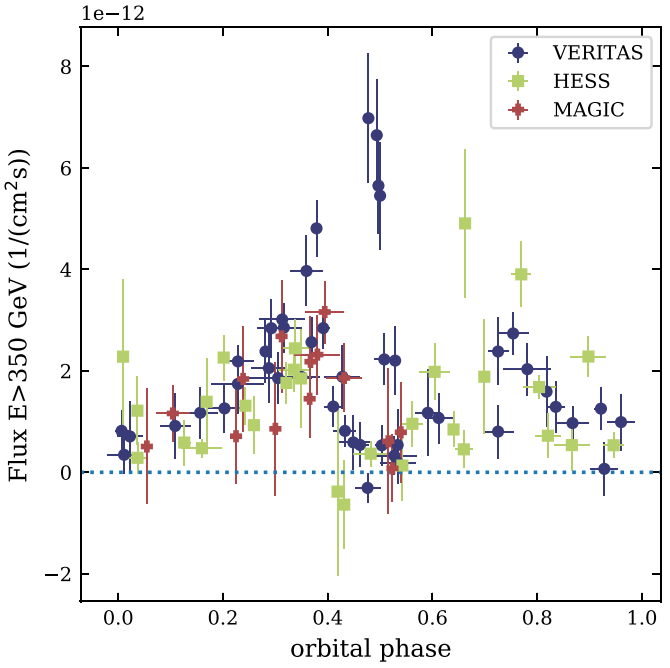

(c) Gamma-rays ($P = 313$ days)

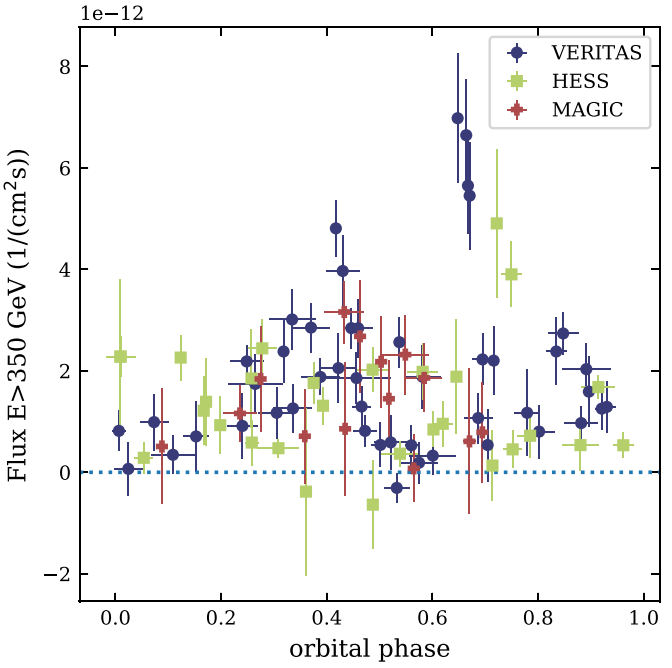

(d) Gamma-rays ($P = 308$ days)

Figure 14. Gamma-ray (>350 GeV) light curves as a function of orbital phase assuming orbital periods as indicated below the plots. For further details, see Figure 3 and text.

would change this picture significantly, because most of the discussed features disappear (Figures 13(d) and 14(d)).

Appendix C
Light Curves per Orbital Cycle

The gamma-ray observations with H.E.S.S., MAGIC, and VERITAS sum up to a total observation time of ≈450 hr spanning 18 orbits of HESS J0632 + 057 covering the period 2004–2019. The X-ray observations by the Swift-XRT, Chandra, XMM-Newton, Suzaku, and NuSTAR are obtained during 14 orbits of the binary system. Despite this large amount of data, there is no good coverage along most of these orbital cycles due to observational constraints and the long binary period of 317 days. This is illustrated in Figures 15 and 16, which show the light curves per orbital cycle at both X-ray and gamma-ray energies assuming an orbital period of 317.3 days.

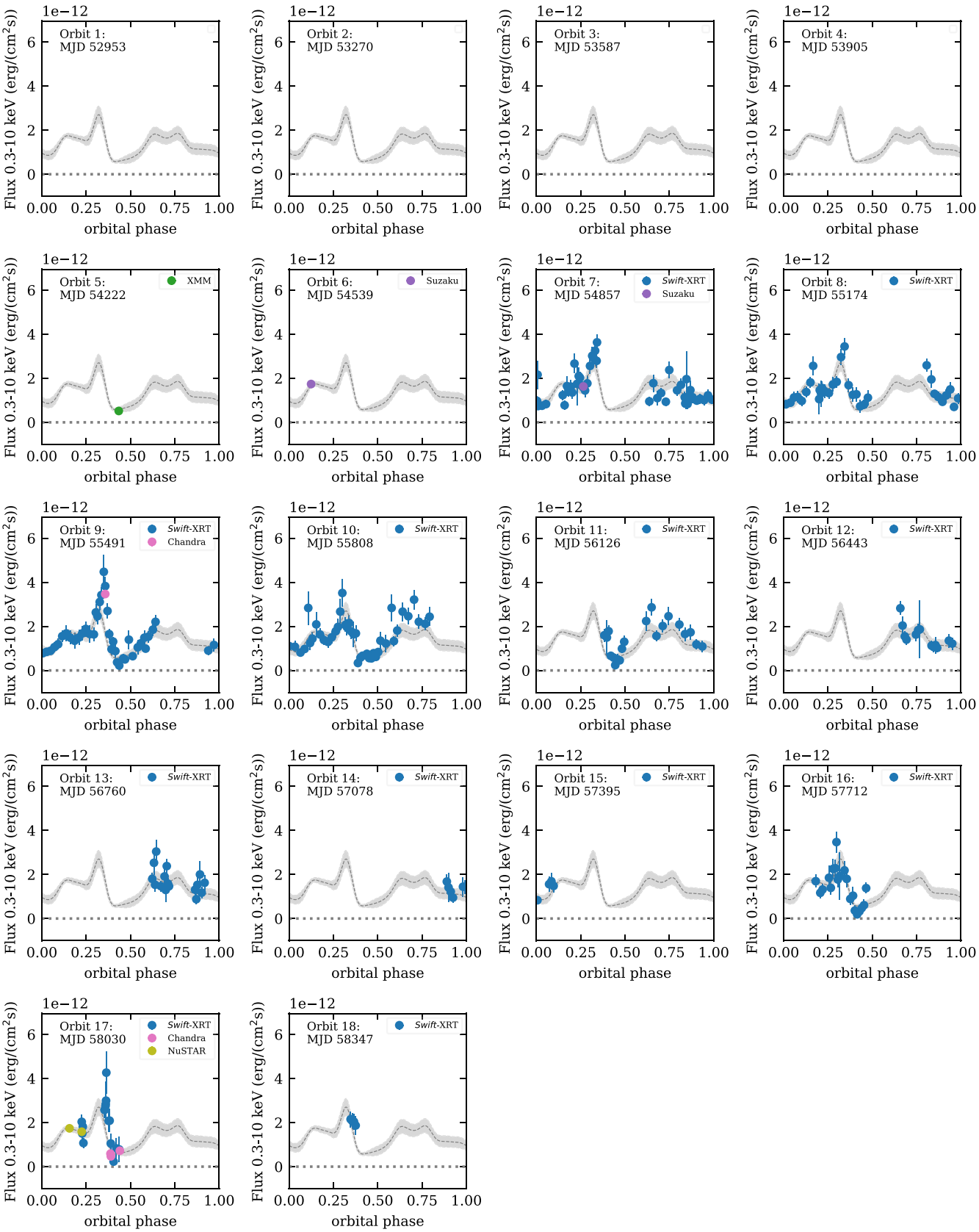

Figure 15. X-ray (0.3–10 keV) light curves as a function of orbital phase for each of the observed orbital cycles. Orbits are numbered following the start of the gamma-ray observations (no X-ray observations are available for the first four orbits; empty panels are shown for easier comparisons with Figure 16). The MJD given in each panel indicates the start of each orbit. An orbital period of 317.3 days is assumed. Vertical lines show statistical uncertainties; note that these are smaller than the marker size for all instruments but Swift-XRT. The thin blue line and gray shaded band in each plot indicates the average Swift-XRT light curve and its 68% containment region calculated from all measurements and smoothed by applying a cubic spline fit.

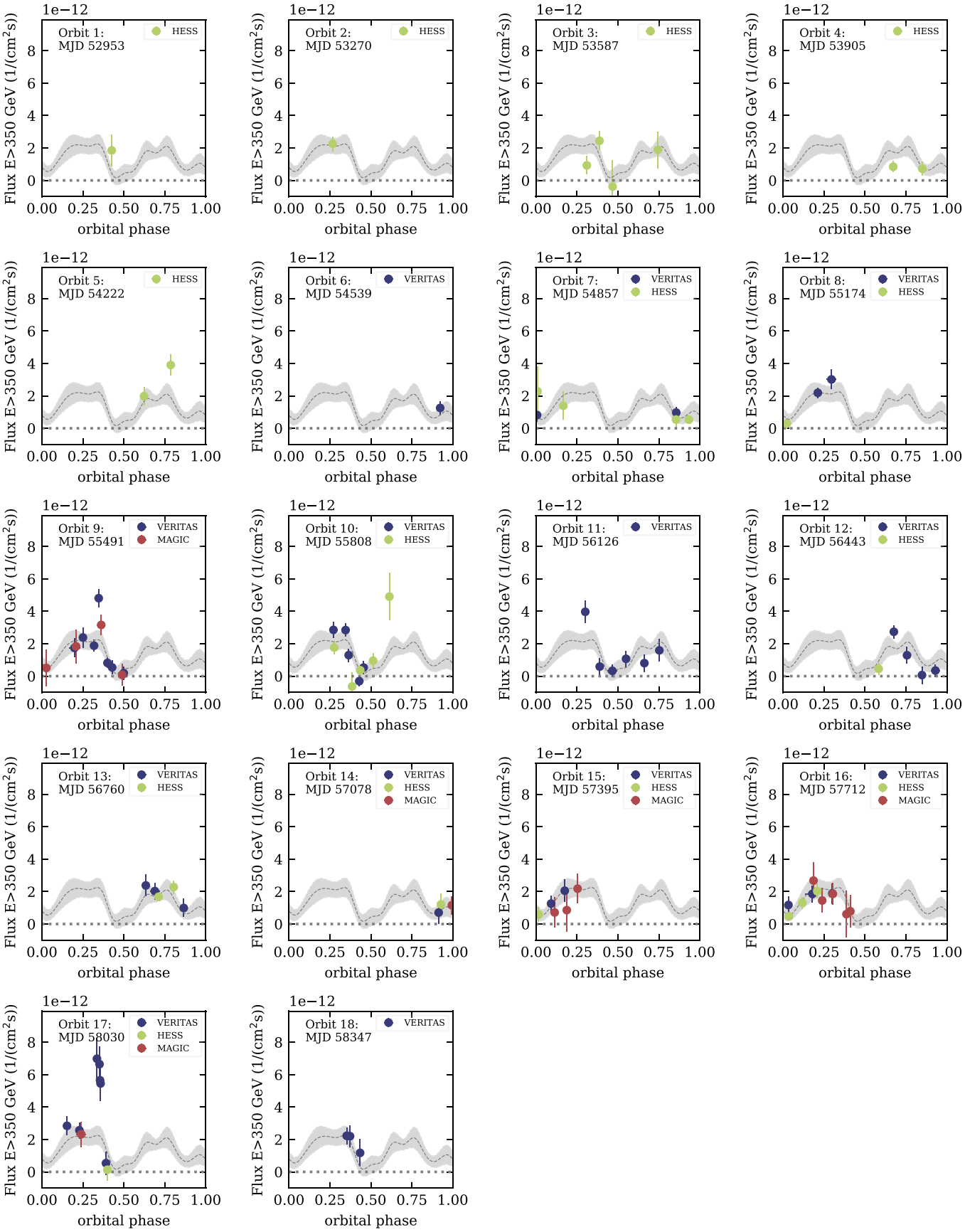

Figure 16. Gamma-ray (>350 GeV) light curves as a function of orbital phase for each of the observed orbital cycles (see Figure 15 for further details). The thin blue line and gray shaded band in each plot indicate the average gamma-ray light curve and its 68% containment region calculated from all measurements and smoothed by applying a cubic spline fit.

Appendix D
Contemporaneous Spectral Energy Distributions

Contemporaneous X-ray and gamma-ray spectral energy distributions for 38 periods of VERITAS and Swift-XRT observations are available through the Zenodo data repository.[127]

ORCID iDs

W. Benbow https://orcid.org/0000-0003-2098-170X
M. Errando https://orcid.org/0000-0002-1853-863X
A. Falcone https://orcid.org/0000-0002-5068-7344
L. Fortson https://orcid.org/0000-0002-1067-8558
A. Furniss https://orcid.org/0000-0003-1614-1273
G. H. Gillanders https://orcid.org/0000-0001-8763-6252
O. Gueta https://orcid.org/0000-0002-9440-2398
D. Hanna https://orcid.org/0000-0002-8513-5603
T. Hassan https://orcid.org/0000-0002-4758-9196
O. Hervet https://orcid.org/0000-0003-3878-1677
B. Hona https://orcid.org/0000-0002-7609-343X
W. Jin https://orcid.org/0000-0002-1089-1754
P. Kaaret https://orcid.org/0000-0002-3638-0637
D. Kieda https://orcid.org/0000-0003-4785-0101
T. K Kleiner https://orcid.org/0000-0002-4260-9186
M. J. Lang https://orcid.org/0000-0003-4641-4201
G. Maier https://orcid.org/0000-0001-9868-4700
P. Moriarty https://orcid.org/0000-0002-1499-2667
R. Mukherjee https://orcid.org/0000-0002-3223-0754
D. Nieto https://orcid.org/0000-0003-3343-0755
M. Nievas-Rosillo https://orcid.org/0000-0002-8321-9168
S. O'Brien https://orcid.org/0000-0002-9296-2981
R. A. Ong https://orcid.org/0000-0002-4837-5253
A. N. Otte https://orcid.org/0000-0002-5955-6383
N. Park https://orcid.org/0000-0002-4282-736X
K. Pfrang https://orcid.org/0000-0002-7990-7179
A. Pichel https://orcid.org/0000-0002-9955-901X
M. Pohl https://orcid.org/0000-0002-5680-0766
J. Quinn https://orcid.org/0000-0002-4855-2694
K. Ragan https://orcid.org/0000-0002-5351-3323
D. Ribeiro https://orcid.org/0000-0002-7523-7366
J. L. Ryan https://orcid.org/0000-0001-6662-5925
M. Santander https://orcid.org/0000-0001-7297-8217
D. Tak https://orcid.org/0000-0002-9852-2469
D. A. Williams https://orcid.org/0000-0003-2740-9714
V. A. Acciari https://orcid.org/0000-0001-8307-2007
S. Ansoldi https://orcid.org/0000-0002-5613-7693
L. A. Antonelli https://orcid.org/0000-0002-5037-9034
A. Arbet Engels https://orcid.org/0000-0001-9076-9582
M. Artero https://orcid.org/0000-0002-4899-8127
K. Asano https://orcid.org/0000-0001-9064-160X
D. Baack https://orcid.org/0000-0002-2311-4460
A. Babić https://orcid.org/0000-0002-1444-5604
A. Baquero https://orcid.org/0000-0002-1757-5826
U. Barres de Almeida https://orcid.org/0000-0001-7909-588X
J. A. Barrio https://orcid.org/0000-0002-0965-0259
I. Batković https://orcid.org/0000-0002-1209-2542
J. Becerra González https://orcid.org/0000-0002-6729-9022
W. Bednarek https://orcid.org/0000-0003-0605-108X
E. Bernardini https://orcid.org/0000-0003-3108-1141
A. Berti https://orcid.org/0000-0003-0396-4190
W. Bhattacharyya https://orcid.org/0000-0003-4751-0414
C. Bigongiari https://orcid.org/0000-0003-3293-8522
A. Biland https://orcid.org/0000-0002-1288-833X
O. Blanch https://orcid.org/0000-0002-8380-1633
G. Bonnoli https://orcid.org/0000-0003-2464-9077
Ž. Bošnjak https://orcid.org/0000-0001-6536-0320
G. Busetto https://orcid.org/0000-0002-2687-6380
R. Carosi https://orcid.org/0000-0002-4137-4370
G. Ceribella https://orcid.org/0000-0002-9768-2751
M. Cerruti https://orcid.org/0000-0001-7891-699X
Y. Chai https://orcid.org/0000-0003-2816-2821
A. Chilingarian https://orcid.org/0000-0002-2018-9715
S. M. Colak https://orcid.org/0000-0001-7793-3106
E. Colombo https://orcid.org/0000-0002-3700-3745
J. L. Contreras https://orcid.org/0000-0001-7282-2394
J. Cortina https://orcid.org/0000-0003-4576-0452
S. Covino https://orcid.org/0000-0001-9078-5507
G. D'Amico https://orcid.org/0000-0001-6472-8381
V. D'Elia https://orcid.org/0000-0002-7320-5862
P. Da Vela https://orcid.org/0000-0003-0604-4517
F. Dazzi https://orcid.org/0000-0001-5409-6544
A. De Angelis https://orcid.org/0000-0002-3288-2517
B. De Lotto https://orcid.org/0000-0003-3624-4480
M. Delfino https://orcid.org/0000-0002-9468-4751
J. Delgado https://orcid.org/0000-0002-0166-5464
C. Delgado Mendez https://orcid.org/0000-0002-7014-4101
D. Depaoli https://orcid.org/0000-0002-2672-4141
F. Di Pierro https://orcid.org/0000-0003-4861-432X
L. Di Venere https://orcid.org/0000-0003-0703-824X
E. Do Souto Espiñeira https://orcid.org/0000-0001-6974-2676
D. Dominis Prester https://orcid.org/0000-0002-9880-5039
A. Donini https://orcid.org/0000-0002-3066-724X
D. Dorner https://orcid.org/0000-0001-8823-479X
M. Doro https://orcid.org/0000-0001-9104-3214
D. Elsaesser https://orcid.org/0000-0001-6796-3205
V. Fallah Ramazani https://orcid.org/0000-0001-8991-7744
A. Fattorini https://orcid.org/0000-0002-1056-9167
M. V. Fonseca https://orcid.org/0000-0003-2235-0725
L. Font https://orcid.org/0000-0003-2109-5961
C. Fruck https://orcid.org/0000-0001-5880-7518
S. Fukami https://orcid.org/0000-0003-4025-7794
Y. Fukazawa https://orcid.org/0000-0002-0921-8837
R. J. García López https://orcid.org/0000-0002-8204-6832
M. Garczarczyk https://orcid.org/0000-0002-0445-4566
M. Gaug https://orcid.org/0000-0001-8442-7877
N. Giglietto https://orcid.org/0000-0002-9021-2888
F. Giordano https://orcid.org/0000-0002-8651-2394
P. Gliwny https://orcid.org/0000-0002-4183-391X
N. Godinović https://orcid.org/0000-0002-4674-9450
J. G. Green https://orcid.org/0000-0002-1130-6692
D. Green https://orcid.org/0000-0003-0768-2203
D. Hadasch https://orcid.org/0000-0001-8663-6461
A. Hahn https://orcid.org/0000-0003-0827-5642
L. Heckmann https://orcid.org/0000-0002-6653-8407
J. Herrera https://orcid.org/0000-0002-3771-4918
J. Hoang https://orcid.org/0000-0001-5591-5927
D. Hrupec https://orcid.org/0000-0002-7027-5021
M. Hütten https://orcid.org/0000-0002-2133-5251
T. Inada https://orcid.org/0000-0002-6923-9314
I. Jiménez Martínez https://orcid.org/0000-0003-2150-6919
L. Jouvin https://orcid.org/0000-0001-5119-8537
M. Karjalainen https://orcid.org/0000-0003-0751-3231

[127] https://doi.org/10.5281/zenodo.5157848

D. Kerszberg https://orcid.org/0000-0002-5289-1509
Y. Kobayashi https://orcid.org/0000-0001-5551-2845
H. Kubo https://orcid.org/0000-0001-9159-9853
J. Kushida https://orcid.org/0000-0002-8002-8585
A. Lamastra https://orcid.org/0000-0003-2403-913X
D. Lelas https://orcid.org/0000-0002-8269-5760
F. Leone https://orcid.org/0000-0001-7626-3788
E. Lindfors https://orcid.org/0000-0002-9155-6199
L. Linhoff https://orcid.org/0000-0001-6330-7286
S. Lombardi https://orcid.org/0000-0002-6336-865X
F. Longo https://orcid.org/0000-0003-2501-2270
R. López-Coto https://orcid.org/0000-0002-3882-9477
M. López-Moya https://orcid.org/0000-0002-8791-7908
A. López-Oramas https://orcid.org/0000-0003-4603-1884
S. Loporchio https://orcid.org/0000-0003-4457-5431
B. Machado de Oliveira Fraga https://orcid.org/0000-0002-6395-3410
C. Maggio https://orcid.org/0000-0003-0670-7771
P. Majumdar https://orcid.org/0000-0002-5481-5040
M. Makariev https://orcid.org/0000-0002-1622-3116
M. Mallamaci https://orcid.org/0000-0003-4068-0496
G. Maneva https://orcid.org/0000-0002-5959-4179
M. Manganaro https://orcid.org/0000-0003-1530-3031
K. Mannheim https://orcid.org/0000-0002-2950-6641
M. Mariotti https://orcid.org/0000-0003-3297-4128
M. Martínez https://orcid.org/0000-0002-9763-9155
D. Mazin https://orcid.org/0000-0002-2010-4005
S. Mender https://orcid.org/0000-0002-0755-0609
S. Mićanović https://orcid.org/0000-0002-0076-3134
D. Miceli https://orcid.org/0000-0002-2686-0098
T. Miener https://orcid.org/0000-0003-1821-7964
J. M. Miranda https://orcid.org/0000-0002-1472-9690
R. Mirzoyan https://orcid.org/0000-0003-0163-7233
E. Molina https://orcid.org/0000-0003-1204-5516
A. Moralejo https://orcid.org/0000-0002-1344-9080
D. Morcuende https://orcid.org/0000-0001-9400-0922
V. Moreno https://orcid.org/0000-0002-8358-2098
E. Moretti https://orcid.org/0000-0001-5477-9097
T. Nakamori https://orcid.org/0000-0002-7308-2356
L. Nava https://orcid.org/0000-0001-5960-0455
V. Neustroev https://orcid.org/0000-0003-4772-595X
C. Nigro https://orcid.org/0000-0001-8375-1907
K. Nilsson https://orcid.org/0000-0002-1445-8683
K. Nishijima https://orcid.org/0000-0002-1830-4251
K. Noda https://orcid.org/0000-0003-1397-6478
S. Nozaki https://orcid.org/0000-0002-6246-2767
Y. Ohtani https://orcid.org/0000-0001-7042-4958
T. Oka https://orcid.org/0000-0002-9924-9978
J. Otero-Santos https://orcid.org/0000-0002-4241-5875
S. Paiano https://orcid.org/0000-0002-2239-3373
M. Palatiello https://orcid.org/0000-0002-4124-5747
D. Paneque https://orcid.org/0000-0002-2830-0502
R. Paoletti https://orcid.org/0000-0003-0158-2826
J. M. Paredes https://orcid.org/0000-0002-1566-9044
L. Pavletić https://orcid.org/0000-0002-9926-0405
P. Peñil https://orcid.org/0000-0003-3741-9764
M. Persic https://orcid.org/0000-0003-1853-4900
P. G. Prada Moroni https://orcid.org/0000-0001-9712-9916
E. Prandini https://orcid.org/0000-0003-4502-9053
C. Priyadarshi https://orcid.org/0000-0002-9160-9617
I. Puljak https://orcid.org/0000-0001-7387-3812
W. Rhode https://orcid.org/0000-0003-2636-5000
M. Ribó https://orcid.org/0000-0002-9931-4557
J. Rico https://orcid.org/0000-0003-4137-1134
C. Righi https://orcid.org/0000-0002-1218-9555
A. Rugliancich https://orcid.org/0000-0001-5471-4701
L. Saha https://orcid.org/0000-0002-3171-5039
N. Sahakyan https://orcid.org/0000-0003-2011-2731
T. Saito https://orcid.org/0000-0001-6201-3761
S. Sakurai https://orcid.org/0000-0001-7427-4520
K. Satalecka https://orcid.org/0000-0002-7669-266X
F. G. Saturni https://orcid.org/0000-0002-1946-7706
B. Schleicher https://orcid.org/0000-0001-8624-8629
K. Schmidt https://orcid.org/0000-0002-9883-4454
J. Sitarek https://orcid.org/0000-0002-1659-5374
D. Sobczynska https://orcid.org/0000-0003-4973-7903
A. Spolon https://orcid.org/0000-0001-8770-9503
A. Stamerra https://orcid.org/0000-0002-9430-5264
J. Strišković https://orcid.org/0000-0003-2902-5044
D. Strom https://orcid.org/0000-0003-2108-3311
M. Strzys https://orcid.org/0000-0001-5049-1045
Y. Suda https://orcid.org/0000-0002-2692-5891
M. Takahashi https://orcid.org/0000-0002-0574-6018
F. Tavecchio https://orcid.org/0000-0003-0256-0995
P. Temnikov https://orcid.org/0000-0002-9559-3384
T. Terzić https://orcid.org/0000-0002-4209-3407
A. Tutone https://orcid.org/0000-0002-2840-0001
J. van Scherpenberg https://orcid.org/0000-0002-6173-867X
G. Vanzo https://orcid.org/0000-0003-1539-3268
M. Vazquez Acosta https://orcid.org/0000-0002-2409-9792
S. Ventura https://orcid.org/0000-0001-7065-5342
V. Verguilov https://orcid.org/0000-0001-7911-1093
C. F. Vigorito https://orcid.org/0000-0002-0069-9195
V. Vitale https://orcid.org/0000-0001-8040-7852
I. Vovk https://orcid.org/0000-0003-3444-3830
M. Will https://orcid.org/0000-0002-7504-2083
C. Wunderlich https://orcid.org/0000-0002-9604-7836
T. Yamamoto https://orcid.org/0000-0001-9734-8203
D. Zarić https://orcid.org/0000-0001-5763-9487
F. Aharonian https://orcid.org/0000-0003-1157-3915
H. Ashkar https://orcid.org/0000-0002-2153-1818
M. Backes https://orcid.org/0000-0002-9326-6400
V. Barbosa Martins https://orcid.org/0000-0002-5085-8828
D. Berge https://orcid.org/0000-0002-2918-1824
K. Bernlöhr https://orcid.org/0000-0001-8065-3252
M. Böttcher https://orcid.org/0000-0002-8434-5692
C. Boisson https://orcid.org/0000-0001-5893-1797
M. Breuhaus https://orcid.org/0000-0003-0268-5122
F. Brun https://orcid.org/0000-0003-0770-9007
T. Bulik https://orcid.org/0000-0003-2045-4803
S. Caroff https://orcid.org/0000-0002-1103-130X
S. Casanova https://orcid.org/0000-0002-6144-9122
A. Chen https://orcid.org/0000-0001-6425-5692
G. Cotter https://orcid.org/0000-0002-9975-1829
J. Damascenev Mbarubucyeye https://orcid.org/0000-0002-4991-6576
G. Fichet de Clairfontaine https://orcid.org/0000-0003-1143-3883
G. Fontaine https://orcid.org/0000-0002-2357-1012
S. Funk https://orcid.org/0000-0002-2012-0080
G. Giavitto https://orcid.org/0000-0002-7629-6499
D. Glawion https://orcid.org/0000-0003-4865-7696
J. F. Glicenstein https://orcid.org/0000-0003-2581-1742
M.-H. Grondin https://orcid.org/0000-0002-8383-251X

T. L. Holch https://orcid.org/0000-0001-5161-1168
M. Jamrozy https://orcid.org/0000-0002-0870-7778
V. Joshi https://orcid.org/0000-0003-4467-3621
Nu. Komin https://orcid.org/0000-0003-3280-0582
K. Kosack https://orcid.org/0000-0001-8424-3621
J.-P. Lenain https://orcid.org/0000-0001-7284-9220
F. Leuschner https://orcid.org/0000-0001-9037-0272
A. Luashvili https://orcid.org/0000-0003-4384-1638
J. Mackey https://orcid.org/0000-0002-5449-6131
D. Malyshev https://orcid.org/0000-0002-9102-4854
V. Marandon https://orcid.org/0000-0001-9077-4058
G. Martí-Devesa https://orcid.org/0000-0003-0766-6473
R. Marx https://orcid.org/0000-0002-6557-4924
A. Mitchell https://orcid.org/0000-0003-3631-5648
L. Mohrmann https://orcid.org/0000-0002-9667-8654
A. Montanari https://orcid.org/0000-0002-3620-0173
E. Moulin https://orcid.org/0000-0003-4007-0145
J. Muller https://orcid.org/0000-0003-0004-4110
T. Murach https://orcid.org/0000-0003-1128-5008
J. Niemiec https://orcid.org/0000-0001-6036-8569
S. Ohm https://orcid.org/0000-0002-3474-2243
L. Olivera-Nieto https://orcid.org/0000-0002-9105-0518
M. Ostrowski https://orcid.org/0000-0002-9199-7031
S. Panny https://orcid.org/0000-0001-5770-3805
R. D. Parsons https://orcid.org/0000-0003-3457-9308
G. Peron https://orcid.org/0000-0003-3255-0077
V. Poireau https://orcid.org/0000-0002-4768-0256
G. Pühlhofer https://orcid.org/0000-0003-4632-4644
M. Punch https://orcid.org/0000-0002-4710-2165
P. Reichherzer https://orcid.org/0000-0003-4513-8241
A. Reimer https://orcid.org/0000-0001-8604-7077
O. Reimer https://orcid.org/0000-0001-6953-1385
M. Renaud https://orcid.org/0000-0002-2203-4880
F. Rieger https://orcid.org/0000-0003-1334-2993
C. Romoli https://orcid.org/0000-0003-2541-4499
G. Rowell https://orcid.org/0000-0002-9516-1581
B. Rudak https://orcid.org/0000-0003-0452-3805
E. Ruiz-Velasco https://orcid.org/0000-0001-6939-7825
A. Santangelo https://orcid.org/0000-0003-4187-9560
M. Sasaki https://orcid.org/0000-0001-5302-1866
H. M. Schutte https://orcid.org/0000-0002-1769-5617
U. Schwanke https://orcid.org/0000-0002-1229-278X
F. Schüssler https://orcid.org/0000-0003-1500-6571
J. N. S. Shapopi https://orcid.org/0000-0002-7130-9270
S. Spencer https://orcid.org/0000-0001-5516-1205
T. Tanaka https://orcid.org/0000-0002-4383-0368
R. Terrier https://orcid.org/0000-0002-8219-4667
N. Tsuji https://orcid.org/0000-0001-7209-9204
C. van Eldik https://orcid.org/0000-0001-9669-645X
C. Venter https://orcid.org/0000-0002-2666-4812
J. Vink https://orcid.org/0000-0002-4708-4219
S. J. Wagner https://orcid.org/0000-0002-7474-6062
A. Wierzcholska https://orcid.org/0000-0003-4472-7204
M. Zacharias https://orcid.org/0000-0001-5801-3945
D. Zargaryan https://orcid.org/0000-0002-2876-6433
A. A. Zdziarski https://orcid.org/0000-0002-0333-2452
S. J. Zhu https://orcid.org/0000-0002-6468-8292
S. Zouari https://orcid.org/0000-0002-5333-2004
N. Żywucka https://orcid.org/0000-0003-2644-6441
Y. Moritani https://orcid.org/0000-0003-2541-1052
D. F. Torres https://orcid.org/0000-0002-1522-9065

References

Abdo, A. A., Ackermann, M., Ajello, M., et al. 2009, Sci, 325, 840
Abeysekara, A. U., Benbow, W., Bird, R., et al. 2018, ApJL, 867, L19
Acciari, V. A., Aliu, E., Arlen, T., et al. 2009, ApJL, 698, L94
Acciari, V. A., Aliu, E., Arlen, T., et al. 2011, ApJ, 738, 3
Ackermann, M., Ajello, M., Ballet, J., et al. 2013, ApJL, 773, L35
Aharonian, F., Akhperjanian, A. G., Bazer-Bachi, A. R., et al. 2006, A&A, 457, 899
Aharonian, F. A., Akhperjanian, A. G., Bazer-Bachi, A. R., et al. 2007, A&A, 469, L1
Ahnen, M. L., Ansoldi, S., Antonelli, L. A., et al. 2016, A&A, 591, A76
Ahnen, M. L., Ansoldi, S., Antonelli, L. A., et al. 2017, APh, 94, 29
Albert, J., Aliu, E., Anderhub, H., et al. 2008a, NIMPA, 594, 407
Albert, J., Aliu, E., Anderhub, H., et al. 2008b, NIMPA, 588, 424
Aleksić, J., Alvarez, E. A., Antonelli, L. A., et al. 2012, ApJL, 754, L10
Aleksić, J., Ansoldi, S., Antonelli, L. A., et al. 2016, APh, 72, 76
Alexander, T. 1997, in Astrophysics and Space Science Library, Vol. 218, Astronomical Time Series, ed. D. Maoz, A. Sternberg, & E. M. Leibowitz (Dordrecht: Kluwer), 163
Aliu, E., Archambault, S., Aune, T., et al. 2014, ApJ, 780, 168
An, H., & Romani, R. W. 2017, ApJ, 838, 145
Anderhub, H., Antonelli, L. A., Antoranz, P., et al. 2009, ApJL, 706, L27
Aragona, C., McSwain, M. V., & De Becker, M. 2010, ApJ, 724, 306
Archambault, S., Archer, A., Aune, T., et al. 2016, ApJL, 817, L7
Archambault, S., Archer, A., Benbow, W., et al. 2017, APh, 91, 34
Archer, A., Benbow, W., Bird, R., et al. 2020, ApJ, 888, 115
Arnaud, K. A. 1996, in ASP Conf. Series, Vol. 101, XSPEC: The First Ten Years, ed. G. H. Jacoby & J. Barnes (San Francisco, CA: ASP), 17
Astropy Collaboration, Price-Whelan, A. M., Sipőcz, B. M., et al. 2018, AJ, 156, 123
Astropy Collaboration, Robitaille, T. P., Tollerud, E. J., et al. 2013, A&A, 558, A33
Barkov, M. V., & Bosch-Ramon, V. 2018, MNRAS, 479, 1320
Bednarek, W. 2006, MNRAS, 368, 579
Berge, D., Funk, S., & Hinton, J. 2007, A&A, 466, 1219
Bongiorno, S. D., Falcone, A. D., Stroh, M., et al. 2011, ApJL, 737, L11
Bosch-Ramon, V., Barkov, M. V., Mignone, A., & Bordas, P. 2017, MNRAS, 471, L150
Bosch-Ramon, V., & Khangulyan, D. 2009, IJMPD, 18, 347
Böttcher, M., & Dermer, C. D. 2005, ApJL, 634, L81
Camilo, F., Ray, P. S., Ransom, S. M., et al. 2009, ApJ, 705, 1
Casares, J., Ribó, M., Ribas, I., et al. 2012, MNRAS, 421, 1103
Cash, W. 1979, ApJ, 228, 939
Chernyakova, M., Malyshev, D., Mc Keague, S., et al. 2020, MNRAS, 497, 648
Czesla, S., Schröter, S., Schneider, C. P., et al. 2019, PyA: Python astronomy-related packages, Astrophysics Source Code Library, http://ascl.net/1906.010
de Naurois, M., & Rolland, L. 2009, APh, 32, 231
Dermer, C. D., & Böttcher, M. 2006, ApJ, 643, 1081
Dubus, G. 2013, A&ARv, 21, 64
Dubus, G., Cerutti, B., & Henri, G. 2008, A&A, 477, 691
Dubus, G., Cerutti, B., & Henri, G. 2010, A&A, 516, A18
Edelson, R. A., & Krolik, J. H. 1988, ApJ, 333, 646
Falcone, A., Bongiorno, S., Stroh, M., & Holder, J. 2011, ATel, 3152
Fomin, V. P., Stepanian, A. A., Lamb, R. C., et al. 1994, APh, 2, 137
Fruscione, A., McDowell, J. C., Allen, G. E., et al. 2006, Proc. SPIE, 6270, 62701V
Graham, M. J., Drake, A. J., Djorgovski, S. G., et al. 2013, MNRAS, 434, 3423
Gregory, P. C. 2002, ApJ, 575, 427
HEASARC 2014, HEAsoft: Unified Release of FTOOLS and XANADU, Astrophysics Source Code Library, http://ascl.net/1408.004
H.E.S.S. Collaboration, Abdalla, H., Adam, R., et al. 2020, A&A, 633, A102
Hillas, A. M. 1985, in Proc. from the 19th Int. Cosmic Ray Conf., Vol. 3 (New York: AIP), 443
Hinton, J. A. & the HESS Collaboration 2004, NewAR, 48, 331
Hinton, J. A., Skilton, J. L., Funk, S., et al. 2009, ApJL, 690, L101
Johnston, S., Manchester, R. N., Lyne, A. G., et al. 1992, ApJL, 387, L37
Kambe, E., Yoshida, M., Izumiura, H., et al. 2013, PASJ, 65, 15
Khangulyan, D., Aharonian, F., & Bosch-Ramon, V. 2008, MNRAS, 383, 467

Khangulyan, D., Aharonian, F. A., Bogovalov, S. V., & Ribó, M. 2011, ApJ, 742, 98
Khangulyan, D., Hnatic, S., Aharonian, F., & Bogovalov, S. 2007, MNRAS, 380, 320
Kirk, J. G., Ball, L., & Skjæraasen, O. 1999, APh, 10, 31
Krause, M., Pueschel, E., & Maier, G. 2017, APh, 89, 1
Kravtsov, V., Berdyugin, A. V., Piirola, V., et al. 2020, A&A, 643, A170
Li, J., Torres, D. F., Cheng, K.-S., et al. 2017, ApJ, 846, 169
Li, J., Torres, D. F., Zhang, S., et al. 2011, ApJL, 744, L13
Li, T.-P., & Ma, Y.-Q. 1983, ApJ, 272, 317
Lomb, N. R. 1976, Ap&SS, 39, 447
Maier, G., & Holder, J. 2017, in 35th Int. Cosmic Ray Conf. (ICRC2017) (Trieste: PoS), 747
Maier, G. & VERITAS Collaboration 2017, in 35th Int. Cosmic Ray Conf. (ICRC2017) (Trieste: PoS), 729
Malyshev, D., Chernyakova, M., Santangelo, A., & Pühlhofer, G. 2019, AN, 340, 465
Manset, N., & Donati, J.-F. 2003, Proc. SPIE, 4843, 425
Martí-Devesa, G., & Reimer, O. 2020, A&A, 637, A23
Massi, M., Ribó, M., Paredes, J. M., Peracaula, M., & Estalella, R. 2001, A&A, 376, 217
Mochol, I., & Kirk, J. G. 2014, AN, 335, 256
Moldón, J., Johnston, S., Ribó, M., Paredes, J. M., & Deller, A. T. 2011a, ApJL, 732, L10
Moldón, J., Ribó, M., & Paredes, J. M. 2011b, A&A, 533, L7
Moldon, J., Ribo, M., & Paredes, J. M. 2011, ASSP, 21, 1
Morgan, W. W., Code, A. D., & Whitford, A. E. 1955, ApJS, 2, 41
Moritani, Y., Kawano, T., Chimasu, S., et al. 2018, PASJ, 70, 61
Moritani, Y., Okazaki, A. T., Carciofi, A. C., et al. 2015, ApJL, 804, L32
Nievas, M. & VERITAS Collaboration 2021, in 37th Int. Cosmic Ray Conf. (ICRC2021) (Trieste: PoS)
Papitto, A., Torres, D. F., & Rea, N. 2012, ApJ, 756, 188
Paredes-Fortuny, X., Bosch-Ramon, V., Perucho, M., & Ribó, M. 2015a, A&A, 574, A77
Paredes-Fortuny, X., Ribó, M., Bosch-Ramon, V., et al. 2015b, A&A, 575, L6
Park, N. & VERITAS Collaboration 2015, in Proc. of the 34th Int. Cosmic Ray Conf. (ICRC2015), 34 (Trieste: PoS), 771
Parsons, R. D., & Hinton, J. A. 2014, APh, 56, 26
Rea, N., & Torres, D. F. 2011, ApJL, 737, L12
Robertson, D. R. S., Gallo, L. C., Zoghbi, A., & Fabian, A. C. 2015, MNRAS, 453, 3455
Scargle, J. D. 1982, ApJ, 263, 835
Shafter, A. W., Szkody, P., & Thorstensen, J. R. 1986, ApJ, 308, 765
Skilton, J. L., Pandey-Pommier, M., Hinton, J. A., et al. 2009, MNRAS, 399, 317
Stellingwerf, R. F. 1978, ApJ, 224, 953
Stoyanov, K. A., Zamanov, R. K., & Iliev, I. K. 2018, ATel, 11233, 1
Sushch, I., & van Soelen, B. 2017, ApJ, 837, 175
Timmer, J., & Koenig, M. 1995, A&A, 300, 707
Tody, D. 1986, Proc. SPIE, 627, 733
Tokayer, Y., An, H., Halpern, J., et al. 2021, ApJ, 923, 17
Torres, D. F., Rea, N., Esposito, P., et al. 2012, ApJ, 744, 106
Uttley, P., Edelson, R., McHardy, I. M., Peterson, B. M., & Markowitz, A. 2003, ApJL, 584, L53
Volkov, I., Kargaltsev, O., Younes, G., Hare, J., & Pavlov, G. 2021, ApJ, 915, 61
Weekes, T. C., Badran, H., Biller, S. D., et al. 2002, APh, 17, 221
Weng, S.-S., Pan, Z., Qian, L., et al. 2021, ATel, 14297, 1
Yoneda, H., Makishima, K., Enoto, T., et al. 2020, PhRvL, 125, 111103
Yudin, R. V., Potter, S. B., & Townsend, L. J. 2017, MNRAS, 464, 4325
Zamanov, R. K., Stoyanov, K. A., Mart, J., Marchev, V. D., & Nikolov, Y. M. 2021, AN, 342, 531
Zamanov, R. K., Stoyanov, K. A., Martí, J., et al. 2016, A&A, 593, A97
Zanin, R., Carmona, E., & Sitarek, J. 2013, in 33rd Int. Cosmic Ray Conf. (ICRC2013) (Trieste: PoS), 2937